Tectonics®

RESEARCH ARTICLE
10.1029/2022TC007607

Key Points:

- Switch from transtensional to oblique opening along the rift correlates to lateral steps of rift segments
- At least 30% of extension in magma-poor areas of the depression is accommodated by upper crustal axial faulting
- Characteristics and spatial distribution of axial faulting in the Danakil Depression mimics that observed along seafloor spreading ridges

Supporting Information:

Supporting Information may be found in the online version of this article.

Correspondence to:

G. L. Hurman,
g.l.hurman@soton.ac.uk

Citation:

Hurman, G. L., Keir, D., Bull, J. M., McNeill, L. C., Booth, A. D., & Bastow, I. D. (2023). Quantitative analysis of faulting in the Danakil Depression Rift of Afar: The importance of faulting in the final stages of magma-rich rifting. *Tectonics*, *42*, e2022TC007607. https://doi.org/10.1029/2022TC007607

Received 20 SEP 2022
Accepted 16 MAY 2023

Quantitative Analysis of Faulting in the Danakil Depression Rift of Afar: The Importance of Faulting in the Final Stages of Magma-Rich Rifting

Gareth L. Hurman[1], Derek Keir[1,2], Jonathan M. Bull[1], Lisa C. McNeill[1], Adam D. Booth[3], and Ian D. Bastow[4]

[1]School of Ocean and Earth Science, University of Southampton, Southampton, UK, [2]Dipartimento di Scienze della Terra, Università degli Studi di Firenze, Florence, Italy, [3]School of Earth and Environment, University of Leeds, Leeds, UK, [4]Department of Earth Science and Engineering, Imperial College London, London, UK

Abstract Magmatic intrusion and faulting both accommodate crustal extension in magma-rich rifts. However, quantitative constraints on the contribution of faulting to total extension and along-rift variations of faulting during the final stages of break-up are lacking. We targeted the Danakil Depression (Afar, Ethiopia) to conduct a quantitative, high-resolution study of fault activity and interaction in a magma-rich rift near break-up. Quantitative analysis of >500 rift axis faults, identified using remote sensing data (satellite imagery, DEMs), shows an increase in fault density, length and connectivity away from magmatic segments. Kinematic and earthquake focal mechanism data demonstrate a transition from transtensional opening in the northern and central sub-regions of the rift to oblique opening in the southern Giulietti Plain and Tat-Ali sub-regions. Oblique opening is attributed to the along-axis step between the Erta-Ale and Harak sub-regions. Integration of seismic reflection and borehole data with the mapped faults shows that extension is primarily accommodated by magmatism within the rift center, with faulting more significant toward the ends of the rift. ~30% of crustal extension is accommodated by axial faulting in areas of low magmatism, highlighting the importance of faulting even in the final stages of magma-rich rifting. Comparing our findings with spreading ridge morphology and structure, relevant due to the rift maturity and extensive magmatism, we conclude that the Danakil Depression is in a transitional stage between continental rifting and seafloor spreading. Spatial changes in the importance of faulting and magmatism in accommodating extension, alongside rift morphology, resemble the relationships observed along spreading ridges.

1. Introduction

Continental rifting is a crucial process in the Wilson tectonic cycle, in particular influencing the development of seafloor spreading (e.g., Ebinger, 2005; Whitmarsh et al., 2001). Rift settings host valuable resources (hydrocarbons, mineral deposits) (e.g., Kyser, 2007; Levell et al., 2011; Zou et al., 2015), inform past climatic records (e.g., Haq et al., 1987; Kirschner et al., 2010), in addition to their associated natural hazards (earthquakes and volcanoes) (e.g., Brune, 2016). Globally, the style of rifting is most commonly viewed in a framework of end members (e.g., Franke, 2013; Tugend et al., 2018) in which magma-poor rifts show extension mainly via mechanical extension (faulting and ductile stretching) (e.g., Lavier & Manatschal, 2006; Peron-Pinvidic et al., 2013; Peron-Pinvidic & Manatschal, 2009; Reston, 2009), whereas magma-rich rifts extend mainly via magma intrusion (Buck, 2006; Hayward & Ebinger, 1996). Despite the elegance and simplicity of these end member models, in reality most rifts fall somewhere between these end members, and/or show sometimes strong along rift variation in extensional style (e.g., Bastow et al., 2018; Keir et al., 2015; Shillington et al., 2009). In magma-rich rifts more specifically, the relative importance of faulting and magma intrusion, and their evolution in space and time, remain poorly understood.

Studies at varying spatial and temporal scales have highlighted the importance of faulting in the evolution of various extensional settings for example, East African Rift (Corti, 2009; Dumont et al., 2019; Hayward & Ebinger, 1996), Gulf of Corinth Rift (Nixon et al., 2016; Taylor et al., 2011), Gulf of Suez (Gawthorpe et al., 2003), North Sea (Bell et al., 2014; Cowie et al., 2005), Iceland (Bull et al., 2003; Villemin & Bergerat, 2013). During the early stages of continental break-up, extension is typically accommodated by long (>60 km), large offset (>1 km) border fault systems, before the locus of extension transitions to a narrow zone (~20-km-wide) of deformation (e.g., Ebinger & Casey, 2001; Ebinger et al., 2017; Hayward & Ebinger, 1996). For magma-rich

rifts, both magmatic intrusion and faulting accommodates extension in this narrow deformation zone, which commonly shows ∼50–100-km length scale segmentation along-rift (magmatic segments) (e.g., Ebinger & Casey, 2001; Hayward & Ebinger, 1996). Numerous studies have been conducted looking at faulting and its interaction with magmatism during continental rifting (e.g., Bastow & Keir, 2011; Dumont et al., 2017; Ebinger & Casey, 2001; Hayward & Ebinger, 1996; Muirhead et al., 2016; Rowland et al., 2007). Traditionally interpretations assume that as magma-rich-rift settings mature, the magmatism accommodates greater amounts of extension at the expense of mechanical deformation (Hayward & Ebinger, 1996). However, the importance of faulting in the final stages of magma-rich rifting remains poorly constrained, with the data (e.g., structural geological mapping, seismic reflection and borehole data) required to resolve the fault networks actively undergoing the final stages of continental-ocean transition at a high resolution, a rarity. The Danakil Depression (Northern Afar), located between the Ethiopian Plateau and Danakil Block (Figure 1), is undergoing the final stages of continental break-up, thus providing the ideal natural laboratory to conduct high resolution, quantitative analysis on the architecture, extension and subsidence facilitated by faulting in an active rift setting before seafloor spreading initiates. Additionally, high resolution studies of fault activity in the Danakil Depression are limited to isolated areas, such as the Dallol region (e.g., Bastow et al., 2018), with an integrated study along the entire rift axis of the Depression currently lacking.

2. Geological Background

2.1. The Afar Depression

The Afar region marks the location of the triple junction between the Red Sea, Gulf of Aden and East African rift systems (Figure 1), which have formed as a result of divergence between the Nubian, Somalian and Arabian plates (McKenzie et al., 1970). Prior to the initiation of rifting (ca. 30–40 Ma), the lithosphere beneath Afar was impacted by plume magmatism (e.g., Furman et al., 2006; Hofmann et al., 1997; Rogers et al., 2000; Rooney, 2017; Ukstins et al., 2002). This resulted in the eruption of most of the Ethiopian large igneous province around 30 Ma with rifting initiating in Afar at roughly the same time (Hofmann et al., 1997; Wolfenden et al., 2005). Extension was initially focused along large border faults (>50-km-long) (Ayalew et al., 2006; Wolfenden et al., 2005), which now separate the Ethiopian and Somalian Plateaus from the Afar Depression. In the Gulf of Aden, rifting initiated earlier at ca. 35 Ma (Autin et al., 2010; Leroy et al., 2010), as a result of counterclockwise rotation of the Arabian plate (ArRajehi et al., 2010; Bellahsen et al., 2003). Continued divergence of the Arabian plate resulted in rift propagation toward Afar between 26 and 31 Ma, and subsequently to the Red Sea with extension not starting until ca. 23 Ma (Szymanski et al., 2016). Around 11 Ma the extension in the southernmost Red Sea rift axis jumped laterally from the marine Red Sea to on land in Northern Afar leading to the Danakil Depression becoming the locus of strain (Eagles et al., 2002). This stepping of the rift axis resulted in rotation of the Danakil Block in an anticlockwise fashion, causing the basin to open in a NE direction (McCluskey et al., 2010; Viltres et al., 2020). Since the Quaternary, extension has been mainly localized along magmatic segments in the rift floor (Wolfenden et al., 2005). Current extension in Northern Afar is orientated NE/SW as indicated by Global Positioning System (GPS) measurements (McCluskey et al., 2010; Viltres et al., 2020). Extension rates increase southwards in the Danakil Depression, with a rate of 7 mm/yr at 15°N and increasing to ∼20 mm/yr at 13°N (McCluskey et al., 2010; Viltres et al., 2020) (Figure 1b).

Crustal thickness in the region has been constrained by collating wide-angle controlled-source seismic refraction (Makris & Ginzburg, 1987), receiver functions (Ahmed et al., 2022; Hammond et al., 2011) and inversion of gravity data (Tiberi et al., 2005), all showing consistent results (Figure 2). Regional crustal thicknesses vary from 40 to 45 km beneath the Ethiopian Plateau, 25–30 km beneath the Danakil Block, 25 km beneath central and southern Afar, and as thin as <15 km in the Danakil Depression (Figure 2). Specifically beneath the Danakil Depression, crustal thickness decreases from 20 to 25 km at the southern end (south of 13°N, 200 km along the profile Figures 2b and 2c) to <15 km in the north (north of 13.7°N, 125 km along the profile of Figures 2b and 2c) (Ahmed et al., 2022; Hammond et al., 2011; Maguire et al., 2006; Makris & Ginzburg, 1987; Stuart et al., 2006).

Seismic velocities and layering of the crust beneath the Danakil Depression are consistent with continental crust that has been both stretched and heavily intruded, with V_P/V_S ratios of >1.9 indicating the presence of partial melt (Dugda et al., 2005; Hammond et al., 2011; Makris & Ginzburg, 1987; Tiberi et al., 2005). Seismic refraction and receiver functions in Afar indicate most of the along rift crustal thickness changes are due to variable thinning of the lower crust (Ahmed et al., 2022; Hammond et al., 2011; Makris & Ginzburg, 1987), leading to alternative

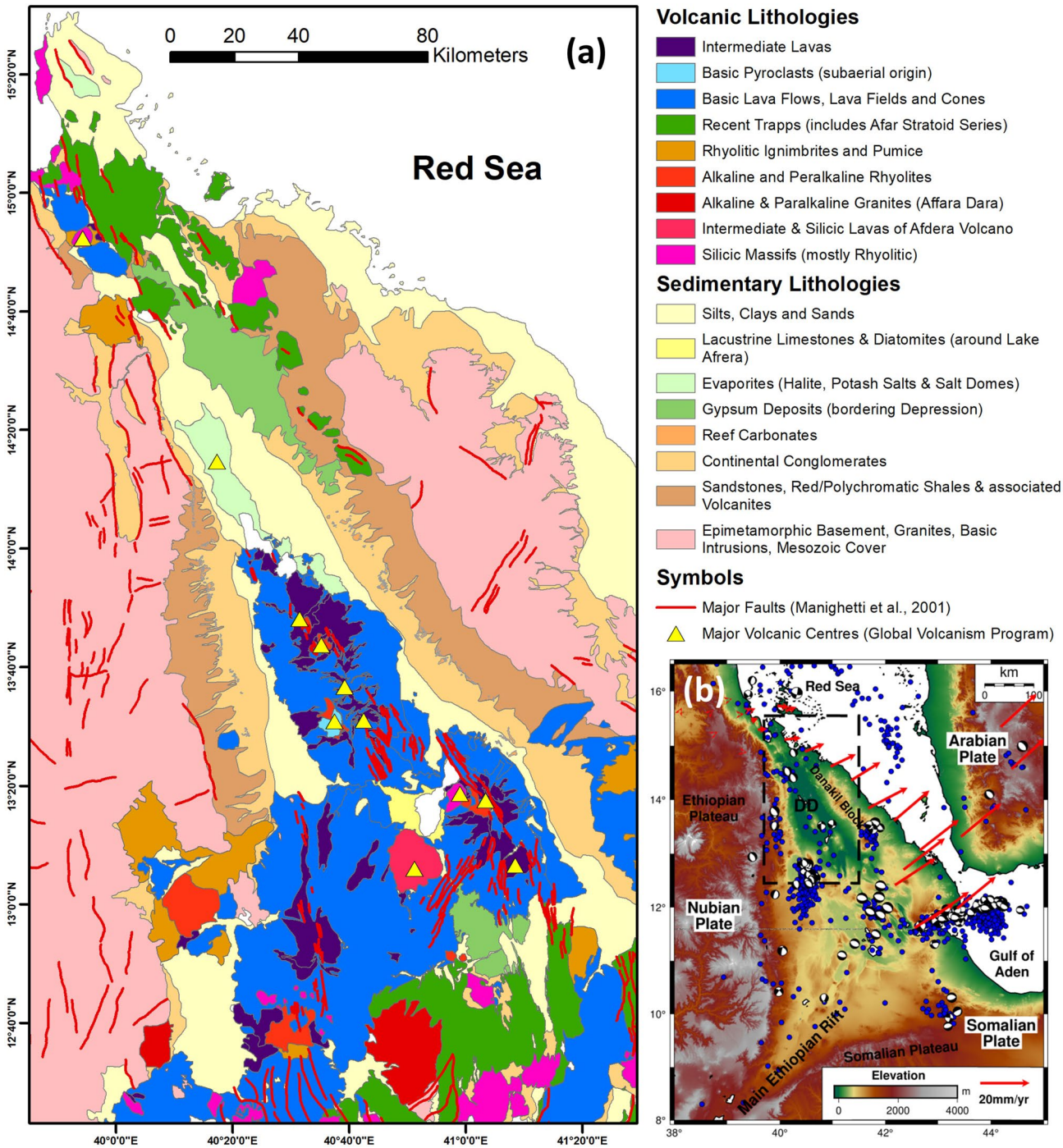

Figure 1. (a) Lithological map of the Danakil Depression produced from multispectral satellite imagery (Landsat 8) and utilizing information in Barberi (1971). Volcanic centers active during the Holocene are marked by yellow triangles (Global Volcanism Program, 2022). (b) Map of the Afar Depression in East Africa, showing the location of the Danakil Depression (DD). Dashed black box shows the location of map (a). Blue dots indicate historic earthquakes (1970–2020) from the NEIC earthquake catalog. Focal mechanisms are taken from the Global CMT catalog. Red vectors, derived from the GPS data of Viltres et al. (2020), show the tectonic extensional direction toward the NE.

interpretations that thinning is either driven by a pure shear style stretching of mainly the lower crust (Bastow & Keir, 2011; Keir et al., 2013), or from simple shear style mid-crustal shear zone detachment faults (Stab et al., 2016). Topography in Afar broadly shows an inverse correlation with crustal thickness, with areas of thicker crust being elevated and thin crust being close to or just below sea level (Figure 2). In addition, the Bouguer

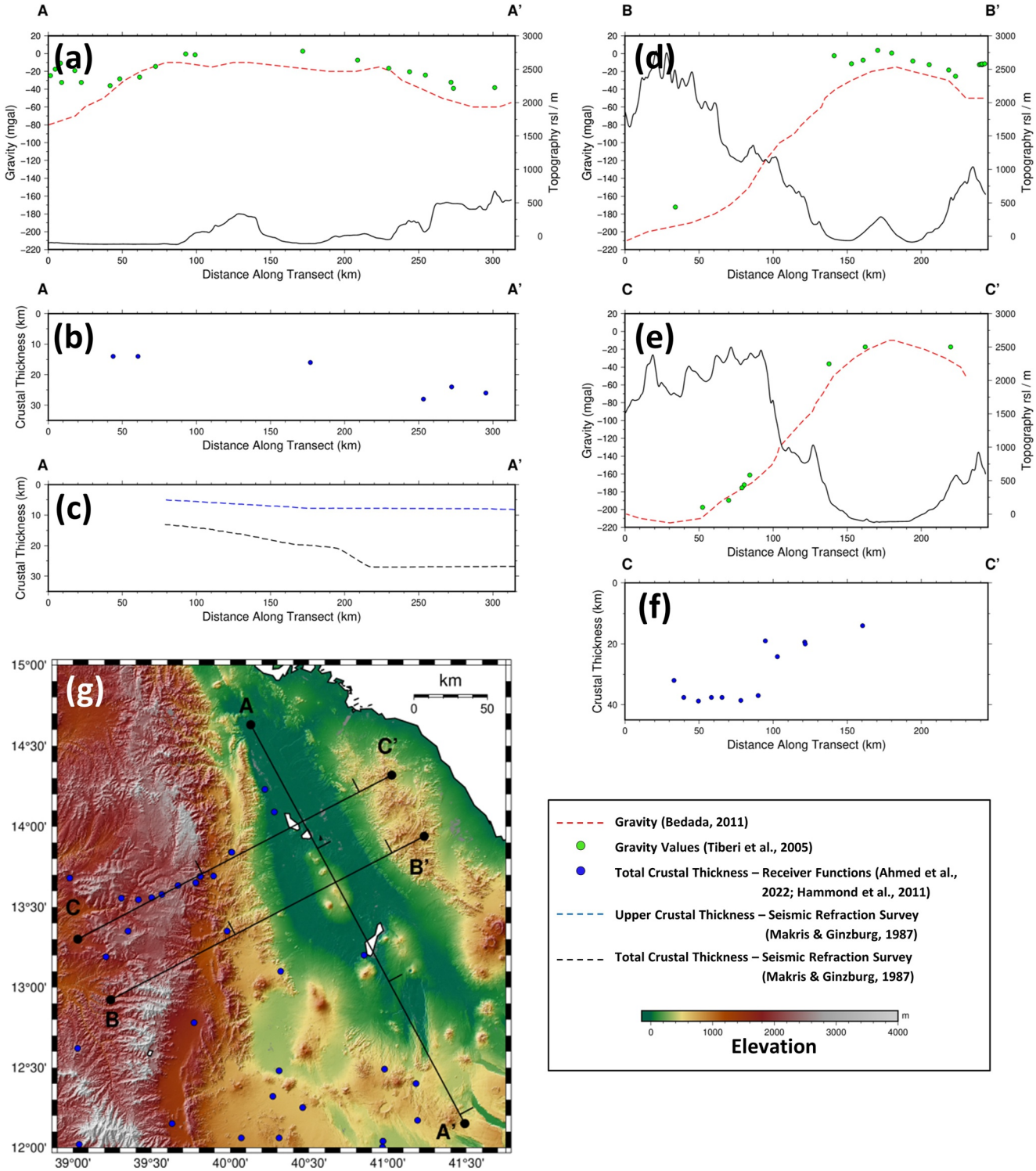

Figure 2. (a) A-A' profile with along axis topography, gravity profile line (dashed red line) from Bedada (2010) and gravity inversion values (green dots) from Tiberi et al. (2005). (b) A-A' axis profile with crustal thickness values derived from receiver functions taken from Ahmed et al. (2022), Hammond et al. (2011) (blue dots). (c) A-A' axis profile with upper crust (blue dashed line) and total crust (black dashed line) thickness values derived from seismic refraction survey (Makris & Ginzburg, 1987). (d) B-B' profile with across axis topography, gravity profile (dashed red line) from Bedada (2010) and gravity inversion values (green dots) from Tiberi et al. (2005). Profile crosses the axis in the Dallol sub-region. (e) C-C' profile with across axis topography, gravity profile (dashed red line) from Bedada (2010) and gravity inversion values (green dots) from Tiberi et al. (2005). Profile crosses the Erta-Ale magmatic segment along the rift axis. (f) C-C' across axis with receiver crustal thickness values from Ahmed et al. (2022), Hammond et al. (2011) (blue dots). (g) Map showing the location of the profiles and receiver function value locations (blue dots). Ticks mark every 100 km along the profiles.

gravity anomaly (which is compensated for topography) also shows an inverse correlation to crustal thickness (Figure 2; Bedada, 2010), strongly suggesting that crustal thickness is the main control on the gravity response.

The mature stage of magma-rich rifting present in Afar provides the ideal location for understanding the importance of faulting during the final stages of break-up. Recent studies in Afar have mainly focused on the central and southern parts of the region (e.g., Dumont et al., 2019; Manighetti et al., 2001), with relatively few constraints on extensional processes just prior to the initiation of seafloor spreading in the Danakil Depression. Therefore this study aims to conduct a high resolution study of rift geometry, kinematics and deformation mode in the Danakil Depression in order to improve our understanding in this key stage of continental breakup. Furthermore, the maturity of the Danakil Depression alongside the high degree of magmatism allows comparison of the faulting and rift morphology in the rift with that present along ocean ridges. This will help to improve our understanding of the onset of seafloor spreading processes as well as how the structure and morphology of extensional settings evolve within the whole rifting process.

2.2. Danakil Depression

The Danakil Depression is approximately 200 km in length and extends from the Gulf of Zula in the north, to the Harak Graben in the south (Figure 3). The Depression is 50–150 km wide, and is bounded on its western margin by the Ethiopian Plateau, which has an Oligo-Miocene border fault system with 3 km of relief (e.g., Keir et al., 2013) (Figures 2 and 3). At the foot of the border faults system lies a series of marginal grabens, 10–20 km wide, with dominantly antithetic faulting (Stab et al., 2016; Tesfaye et al., 2003; Wolfenden et al., 2005; Zwaan, Corti, Sani, et al., 2020). The eastern margin of the basin is defined as the Danakil Block, which has an elevation of 0.5–1 km (e.g., Keir et al., 2013) (Figures 2 and 3). The center of the basin is a locus of young volcanism and faulting defining magmatic segments, with the Erta-Ale magmatic segment in the north and the Tat-Ali magmatic segment in the south (Figure 3) (Barberi & Varet, 1970; Keir et al., 2013).

The Erta-Ale magmatic segment trends NNW-SSE and dominates the central part of the Depression, with a width of 10–20 km and a maximum elevation of 600 m (Barberi & Varet, 1970; Keir et al., 2013; Pagli et al., 2012). A heavily faulted axial graben is absent along the Erta-Ale magmatic segment, in contrast to that observed elsewhere in the Afar region (e.g., Barberi & Varet, 1970; Pagli et al., 2012; Thurmond et al., 2006). Instead several volcanic centers (e.g., Erta-Ale, Tat-Ali, Dallafilla, Gada Ale) form an axial high, with activity dominated by rift aligned dyke intrusions and fissure eruptions (Moore et al., 2019; Nobile et al., 2012; Pagli et al., 2012; Watts et al., 2020; Xu et al., 2017). Located to the SE of the Erta-Ale magmatic segment in a left stepping en-echelon arrangement is the NNW-SSE trending Tat-Ali magmatic segment (Figure 3). The offset region between the magmatic segments is known as the Giulietti Plain (also sometimes called the Afrera Plain) and has been interpreted as a proto-transform fault zone (Bonatti et al., 2017; Illsley-Kemp, Bull, et al., 2018; La Rosa et al., 2019, 2021). NE/SW orientated faults have been observed to the SW of Tat-Ali magmatic segment, which have been attributed to a linkage zone between the Danakil Depression and the Dabbahu-Manda-Hararo rift segment to the SW (Figure 3) (Barberi & Varet, 1977; Schaegis et al., 2021).

A feature of the Danakil Depression is the extensive seismicity and magmatism present which is focused along the magmatic segments (Figure 3) (e.g., Illsley-Kemp, Keir, et al., 2018; Pagli et al., 2012). Additionally, significant earthquake clusters are located at the offsets between en-echelon magmatic segments (Figure 3), including across the Giulietti Plain, where a major cluster of shallow events (<5 km in depth) is located with magnitudes up to 4.2 M_L (Illsley-Kemp, Keir, et al., 2018). However, there are fewer earthquakes at the southern end of the Danakil Depression (south of 13°N) compared with the rest of the rift axis (Figure 3). The western rift margin is also seismically active and accommodates some portion of the extension (Illsley-Kemp, Keir, et al., 2018; Zwaan, Corti, Sani, et al., 2020), with significant seismicity observed between 12.5° and 14°N, along the western marginal graben system (Figure 3).

The oldest lithological unit across the Danakil Depression and the rift margins is the Precambrian Basement, which forms large sections of the bordering Ethiopian Plateau and Danakil Block (Figure 1) (Drury et al., 1994; Ghebreab & Talbot, 2000). Symmetrically fringing the Danakil Depression is the Mio-Pliocene Red Bed Series which is composed of clastic sediments deposited in alluvial conditions (Figure 1) (e.g., Le Gall et al., 2018). The Depression floor is dominated by volcanic units from the active magmatism (Figure 1), with the Erta-Ale and Tat-Ali magmatic segments largely basaltic in composition and 0.6 Ma—present in age (Beyene &

10.1029/2022TC007607

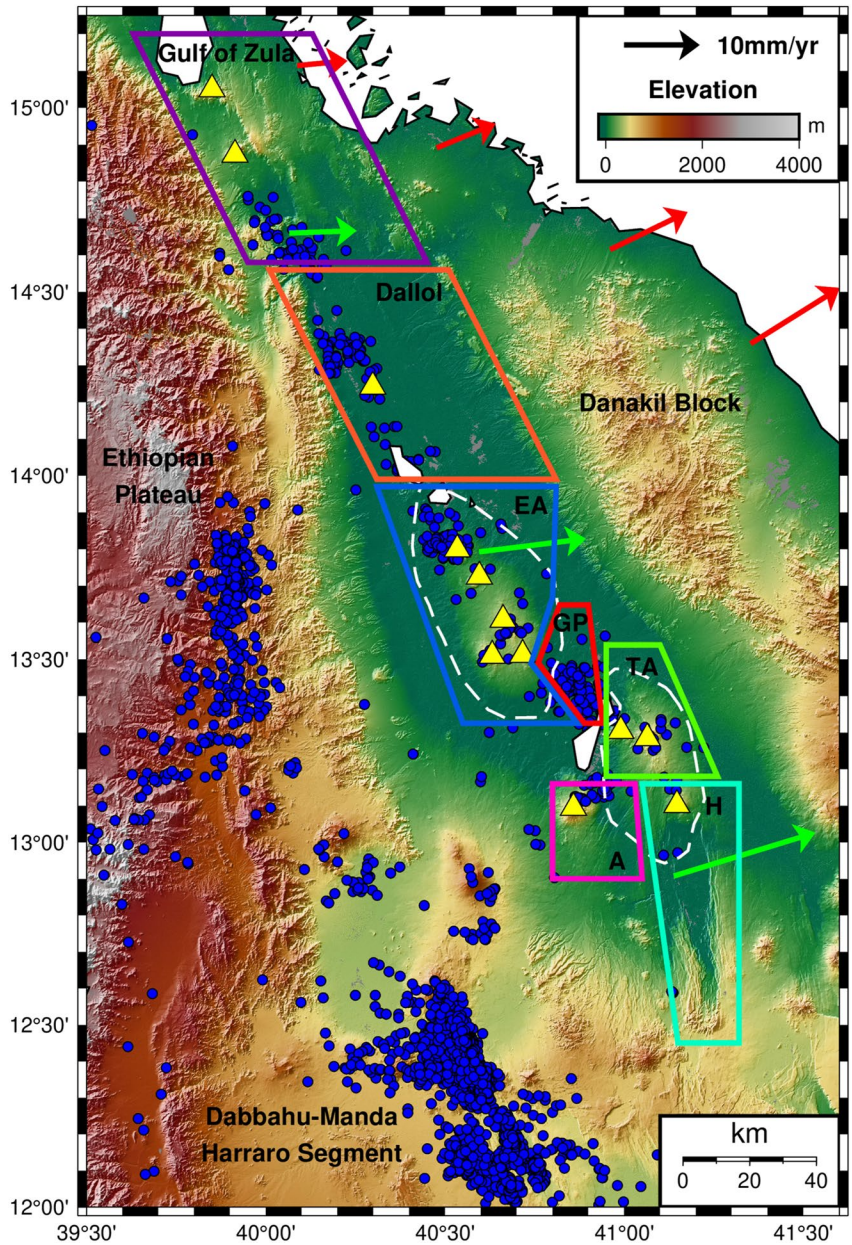

Figure 3. Map of the Danakil Depression study area. Colored boxes show the seven sub-regions the rift axis has been divided into for mapping changes in fault characteristics. Dashed white lines outline the Erta-Ale (north) and Tat-Ali (south) magmatic segments. Red vectors, from GPS recordings, show plate motion along the Eritrean coastline, green vectors from a GPS derived model show the plate motion vector along the rift axis (Viltres et al., 2020). Volcanic centers active during the Holocene marked by yellow triangles (Global Volcanism Program, 2022). Blue dots indicate earthquakes, taken from a regional catalog composed of events from Belachew et al. (2011) and Illsley–Kemp, Keir, et al. (2018). EA = Erta-Ale, GP = Giulietti Plain, TA = Tat-Ali, A = Afdera, H = Harak.

Abdelsalam, 2005; Watts et al., 2020). However, at the southern end of the Danakil Depression the volcanic surface lithology is older with the Afar Stratoid Series (3.5–0.6 Ma) present across the Harak Graben (Beyene & Abdelsalam, 2005) (Figures 1 and 3). With most of the Depression 50–100 m below sea-level (Keir et al., 2013), Pleistocene-Recent evaporitic deposits (dominantly gypsum and halite) cover large parts of the Danakil Depression as a result of marine incursions during high stand periods (Barberi & Varet, 1970; Hutchinson & Engels, 1970). The last period of marine incursion is thought to have occurred 100–120 ka (Marine Isotope Stage 5e) as indicated by dating the youngest unit of the carbonate reef rim present around the rift (Jaramillo-Vogel

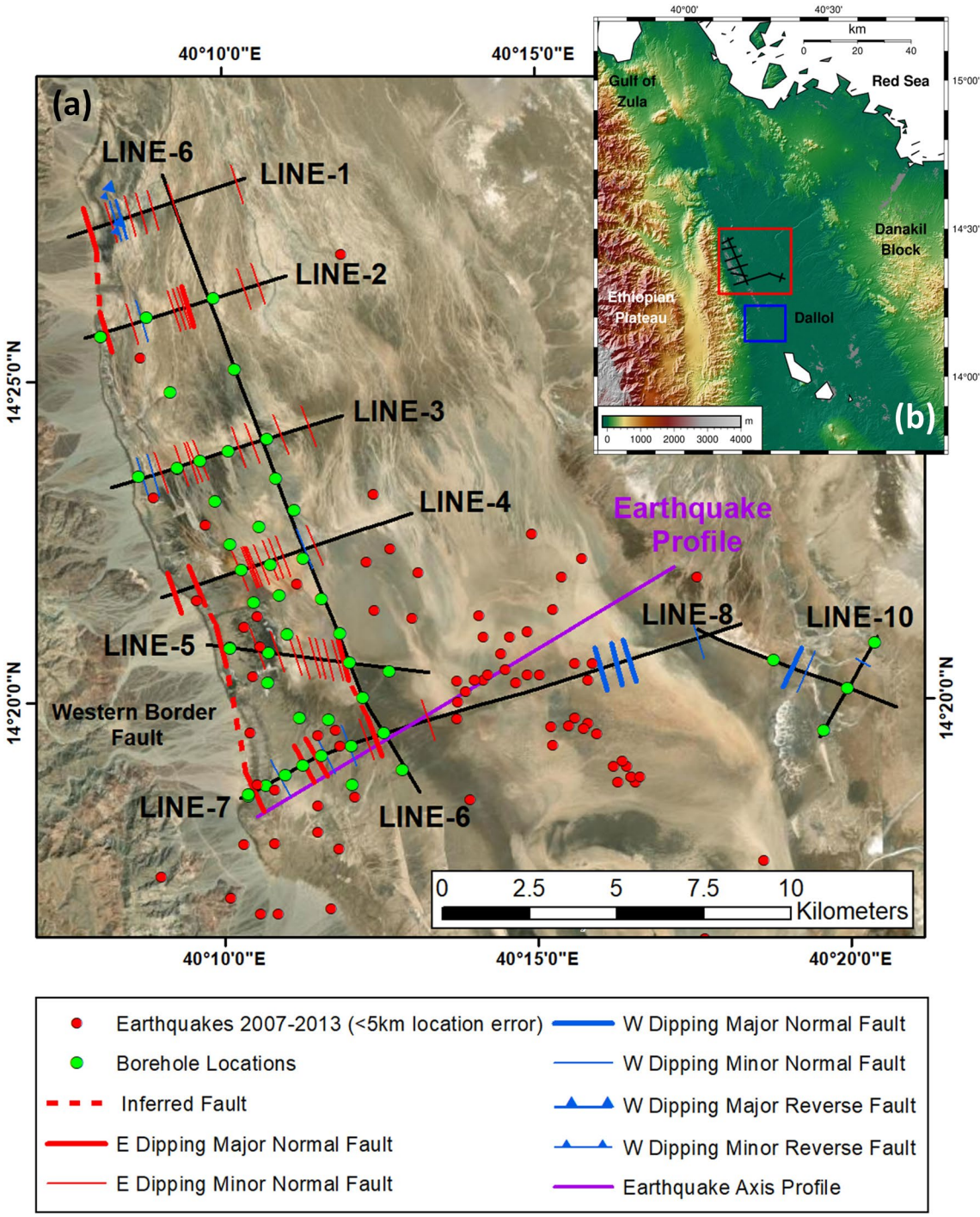

Figure 4. (a) Map showing the location of the seismic lines and boreholes in the Dallol sub-region. The surface is largely covered by evaporite deposits making identifying faults at the surface challenging. Location of where subsurface faults were identified along the seismic lines indicated by ticks. Location of Earthquakes (2007–2013) shown, with only events with <5 km error in location (lat, long and depth) included. Earthquakes are taken from a regional catalog composed of events from Belachew et al. (2011) and Illsley-Kemp, Keir, et al. (2018). (b) Map shows the location of the seismic reflection lines interpreted in this study (red box) in the northern part of the Danakil Depression. The location of seismic reflection lines and boreholes analyzed in the study further south by Bastow et al. (2018) shown by the blue box.

et al., 2019). Active hydrothermal processes in the Dallol sub-region also result in the continuous precipitation of evaporites at the surface of the basin (e.g., López-Garcia et al., 2020) (Figure 4). Therefore, variations in the surface geology along the rift axis are observed, with areas of reduced active surface volcanism, such as the

Dallol sub-region, largely covered by evaporite deposits and a thin veneer (>50 m) of recent alluvial material at the surface (Figure 4). By contrast, along the magmatic segments, the considerable active magmatism has led to lava flows overlying and interbedding with the evaporite deposits.

During the Miocene, extension in Afar generally is thought to have transitioned from being mechanical to magmatically dominated (Ayalew et al., 2006; Wolfenden et al., 2005). However, in the Danakil Depression specifically, the exceptionally thin crust (Figure 2) combined with thick Pliocene-Recent basin fill has led to the hypothesis that here, rapid ductile stretching of the lower crust and significant upper crust faulting may have dominated the last few Myrs of evolution (Bastow et al., 2018; Bastow & Keir, 2011; Keir et al., 2013). Previous studies of faulting in the Danakil Depression have either looked at localized regions within the basin (e.g., Acocella, 2006; Bastow et al., 2018) or been part of a wider regional study resulting in low resolution analysis (e.g., Manighetti et al., 2001). These localized studies highlight the significant upper crustal fault activity in the Danakil Depression, with slip rates of 3.8–5 mm/yr on the western side of the rift floor within the last ∼100 ka, causing rapid subsidence in the Dallol area of the basin (Bastow et al., 2018). Faulting has also been shown to accommodate active extension in the step-over zone between the Erta-Ale and Tat-Ali magmatic segments (Illsley-Kemp, Bull, et al., 2018; La Rosa et al., 2019). Therefore, despite increasing magmatism, upper crustal faulting still contributes significantly to continental break-up and control of the rift structure in the Danakil Depression.

3. Data and Methodology

3.1. Remote Sensing Data and Spatial Analysis

Existing geological maps (Barberi, 1971) were combined with interpretation of Landsat multispectral imagery (Figure 5a) to produce a lithological map of the Danakil Depression (Figure 1), which allows the structural development of the basin to be determined. Additional data sets, including detailed (30 m spatial resolution) Digital Elevation Models (DEMs) in the form of Shuttle Radar Topography Mission (SRTM) and Advanced Spaceborne Thermal Emission and Reflection Radiometer (ASTER), alongside Google Earth Pro, were used to identify and map normal faults and fractures. Hillshade, slope, aspect and curvature functions were applied to the DEMs, enabling structures to be more easily identified (Figure 5b–5f). As a result of the Danakil Depression's size, only faults and fractures visible in satellite imagery at a scale of 1:40,000 were digitized in ArcMap 10.7. Using these methods, 586 structural features (faults and fractures) were identified along the rift axis in the basin (Figure 6a). The mapped structural features will be referred to as faults throughout, although this includes fractures (structures without visible vertical offset). The mapped structures were divided into seven sub-regions (Gulf of Zula, Dallol, Erta-Ale, Giulietti Plain, Tat-Ali, Afdera, Harak sub-regions, see Figure 3) based on changes in the characteristics of the structural features (e.g., orientation, displacement) or the geological setting (e.g., surface lithology type, individual magmatic segments).

Various characteristics of the faults identified in the sub-regions were quantified, enabling comparative analysis of the faulting along the rift axis. The Network GT toolbox (Nyberg et al., 2018) was used in ArcGIS to calculate length-weighted rose diagrams showing the orientation of the faults in each study region (Figure 6a). The dip directions of the axial faults were identified using the aspect and curvature functions in ArcMap (Figure 5d–5f), as well as topographic transects across the structures. Fault density was also calculated using the inbuilt line density tool in ArcMap, with the study area gridded into 1 km^2 regions and a search radius of 1 km from the center point of each region (Figure 6c). Additionally, analysis of fault lengths for each of the sub-regions was conducted with histograms produced and average length values calculated (Figure 6d).

3.1.1. Uncertainties and Errors

Using remote sensing methods to map the faults along the rift axis does have some limitations, which were particularly apparent when mapping structures in the Dallol sub-region. Evaporites, continuously deposited at the surface of the Dallol sub-region (e.g., López-Garcia et al., 2020), obscure the surface rupture and offset of any subsurface faults (Figure 4). Therefore, most of the faults in the Dallol sub-region were inferred from the linear changes in apparent surface lithology (based on color and/or textural change). Additionally, in these cases, characteristics such as dip direction and fault scarp throw values could not be identified and/or quantified. Inference of faulting here means that the fault mapping is likely incomplete in the Dallol sub-region, thus causing a degree of observational bias and making comparative analysis with other sub-regions challenging. Parameters that were particularly impacted by this include fault density, length and connectivity with the topological analysis. For several faults mapped along the axis, the small amount of fault scarp throw made identifying the dip direction of the structures challenging, particularly in the Erta-Ale sub-region.

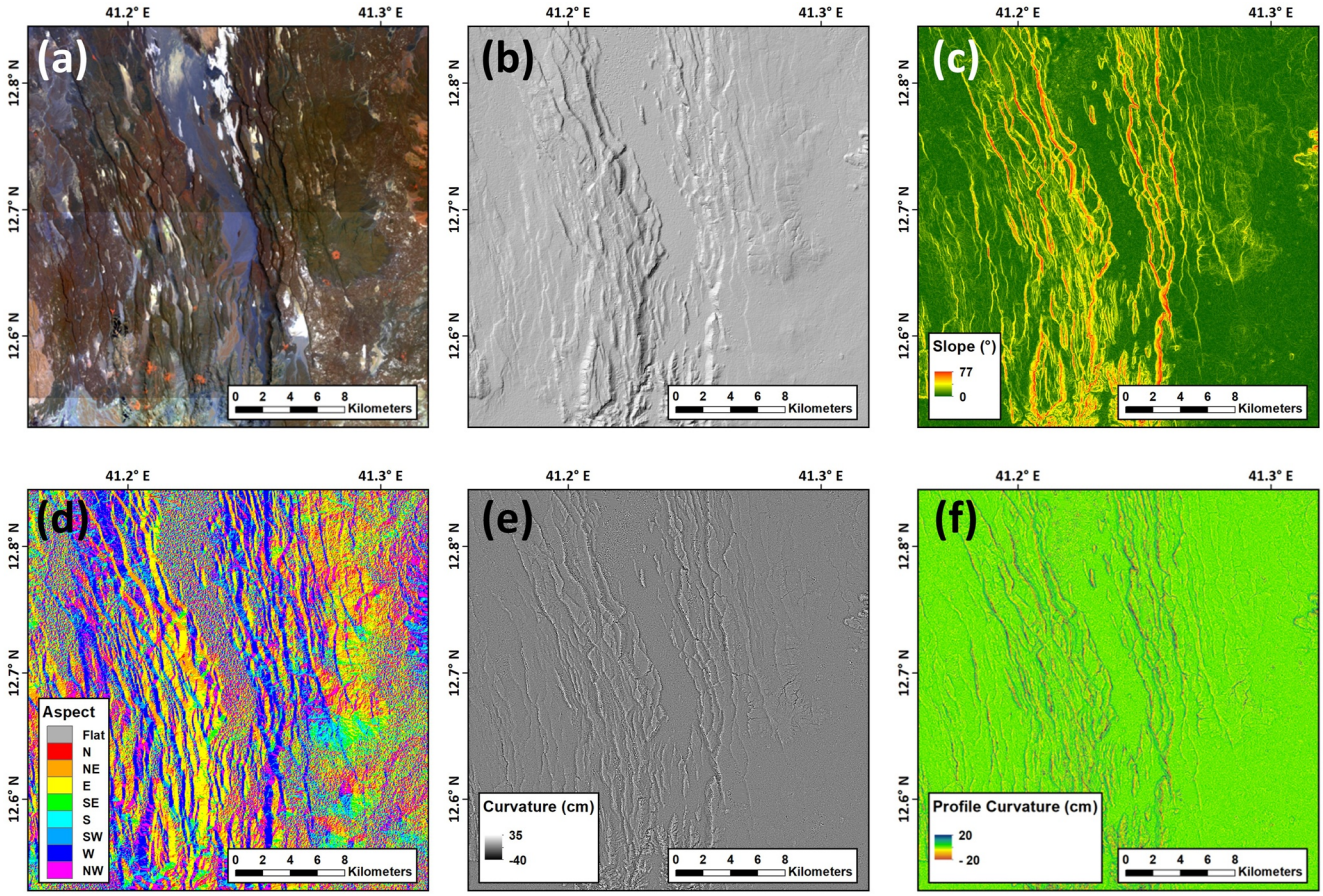

Figure 5. Comparison of quantitative analysis methods applied to the Danakil Depression to identify fault attributes. (a) Multispectral Landsat Imagery. (b) Hillshade—shaded relief created from a DEM. The illumination source for this image is at an azimuth of 315° relative to north. (c) Slope—the maximum gradient of the topography in the center cell, helping to identify fault scarps. (d) Aspect—categorizes the topography into nine classes according to the direction the maximum slope is facing, enabling the fault dip direction to be identified. (e) Curvature—the maximum change in slope of the center cell to its eight neighbors. (f) Profile Curvature—curvature of the topography in the direction of the slope. This enabled identification of scarps with high (blue) and low (red) values representing the convex and concave nature of the hanging wall and foot wall cut offs respectively.

3.2. Fault Topology Analysis

Analysis of the topological characteristics of the fault networks was conducted using the Network GT toolbox (Nyberg et al., 2018) in ArcGIS 10.7. Conducting analysis of the topology of the faulting in each sub-region provides a way of comparing and quantifying fault connectivity and continuity. Fault networks are made up of lines, nodes and branches (Figure 7a). Nodes are the end points of faults or the location of connection between two fault structures, and are classified as either isolated nodes (I-nodes) or connecting nodes (X- and Y-nodes). I-nodes are where an end point of a fault is not connected to another fault structure. X-nodes are where two fault structures cross over each other, whilst a Y-node is where a fault terminates against another fault. Branches are the sections of faults between nodes, and are classified by the node types at either end of the branch. Therefore, they are divided into I-I, I-C, and C-C (I = isolated, C = connected) branch groups. The relative proportion of node and branch types for each sub-region's fault network was then calculated, enabling comparison and quantification of the varying connectivity of the fault structures along the rift axis (Figures 7b and 7c). Inferred mapping of structures, as conducted in the Dallol sub-region will likely mean that numerous faults are not identified resulting in a reduction in the connectivity quantified by the topological analysis in the sub-region.

3.3. Dallol Seismic Reflection and Borehole Data

We interpreted nine 2-D seismic reflection profiles (Figure 4), located in the Dallol sub-region, acquired in 2014 by Tesla Exploration International, using a vibroseis source with a 3 s record length; a sweep frequency of

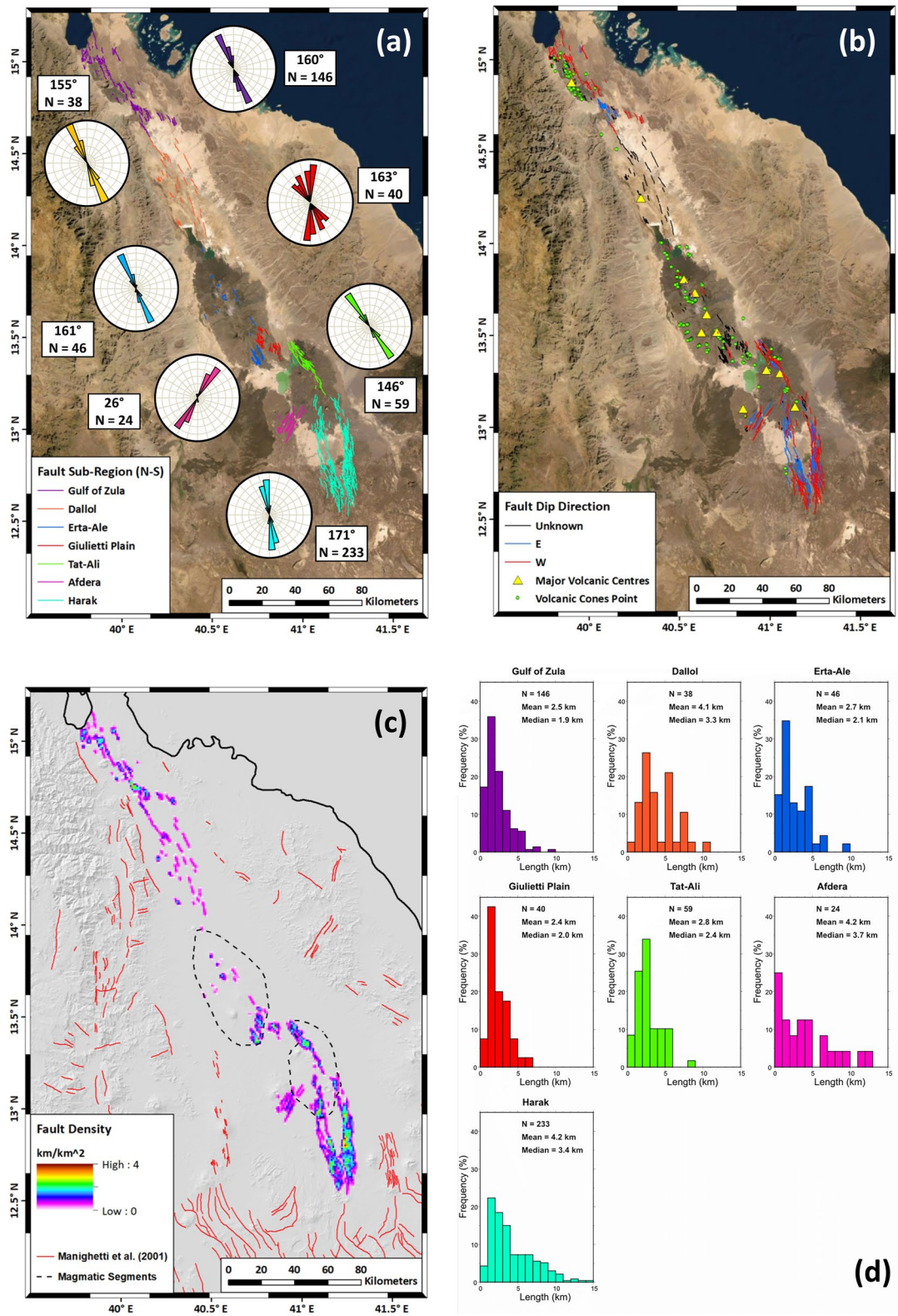

Figure 6.

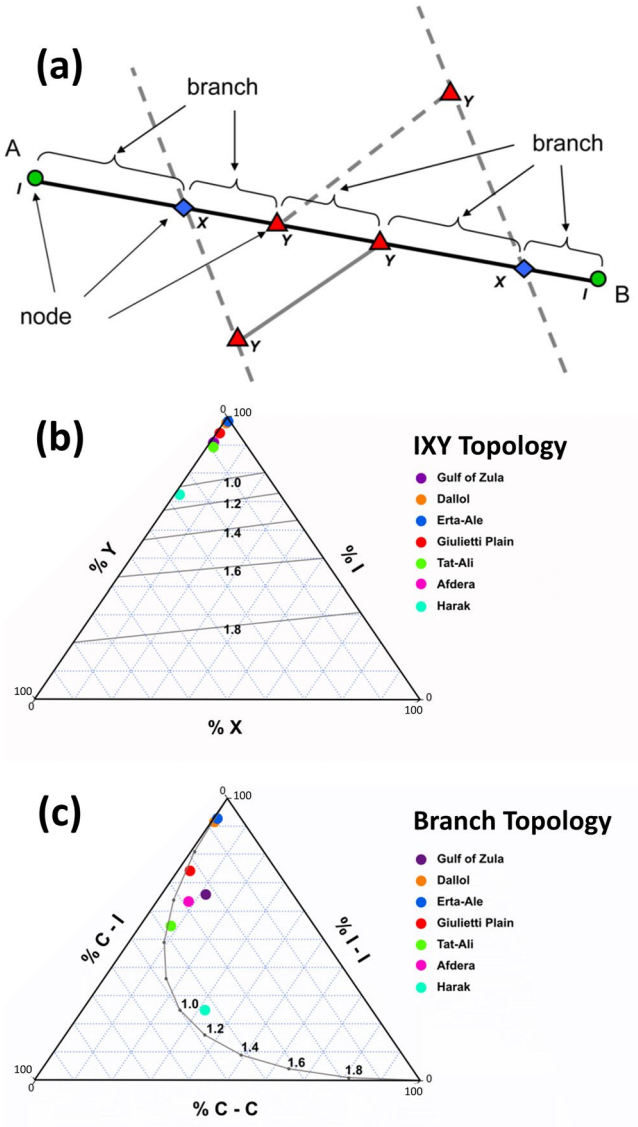

Figure 7. (a) Illustration showing the different types of branches and nodes identified in the fault networks. Fracture trace (A-B) is intersecting with other fractures (dashed), showing arrangement of nodes and branches. I-nodes (circles); Y-nodes (triangles); X-nodes (diamonds). (b) Ternary plot showing the relative proportions of I-, Y- and X-nodes of the fault networks in each sub-region. (c) Ternary plot showing the relative proportion of I-I, C-I and C-C branch types of the fault networks in each sub-region. Contour lines on (b) and (c) show the average number of connections per branch.

8–100 Hz; a source interval of 10 m; a receiver interval of 5 m and a CDP interval of 2.5 m. The lines were processed by Tesla Exploration International in February 2015, using Landmark SeisSpace/ProMAX V5000.0.3.0 processing software and Green Mountain Geophysics (GMG) Millennium Suite refraction statics software. Furthermore, the lines were processed to a datum of ground level at −120 m b. s. l. using a one layer pseudo 3D refraction statics model. Our interpretation approach was to track high amplitude reflectors, with faults and horizons interpreted simultaneously.

Thirty nine boreholes, drilled in 2013 by Terratec Geophysical Services across the site of the seismic reflection lines, were used to help constrain three horizons mapped across the seismic lines (Figure 4). These horizons are A) the base of the Overburden, B) top of the Bischofite unit and C) the base of the Bischofite unit. The unit between the base of the Overburden (Horizon A) and the top of the Bischofite (Horizon B) is known as the Upper Rock Salt (URS), while the Bischofite unit is also known as the Houston Formation (Bastow et al., 2018). Time-depth charts were generated by Tesla Exploration International, converting depth to time using bulk velocities for all the boreholes. Although, there is some uncertainty with this method, the purpose of the seismic reflection and borehole data is to better understand the larger structural features of the rift axis, including slip rates for faults that are identified in the Dallol sub-region, rather than providing detailed constraints on the nature of the sedimentary units. The time-depth charts have been used to constrain the location of the three mapped horizons at borehole locations along the seismic reflection lines.

3.3.1. Fault Throw, Slip and Extension Rates

Velocities for the Overburden and URS (between Horizons A and B) units, taken from Lascialfari (2017), were used to calculate throw values for faults identified along the seismic reflection lines down to Horizon B. Lascialfari (2017) calculated these from stacking velocities and applying Monte Carlo simulation for velocity uncertainty. Velocities for the entire length of seismic line LINE-7 (Figure 4) were calculated using this method, thus enabling throw values to be determined for faults across the rift axis. Because the seismic data are not depth converted, it is difficult to determine accurate fault dips. Therefore, a range of 50–70°, typical for normal faults (Anderson, 1951) was assumed, along with the calculated throw, to produce estimated extension and slip values for the faults. The Bischofite formation was formed at the end of the most recent marine incursion in the Danakil Depression, after which precipitation of the URS unit occurred (Bastow et al., 2018; Foubert et al., 2015a, 2015b; Jaramillo-Vogel et al., 2019). Uranium-dating of corals and bivalves from reef rim carbonates, located around the margins of the Danakil Depression, indicates the last marine incursion was 100–120 ka (Jaramillo-Vogel et al., 2019). Therefore, Horizon B (top of Bischofite formation and base of URS) is assigned this age range, enabling fault slip and extension rates to be calculated over the last ∼100 ka across the rift.

3.4. Earthquake Focal Mechanism Data

Focal mechanisms from the Global Centroid Moment Tensor (CMT) Project (Dziewonski et al., 1981; Ekström et al., 2012) catalog were gathered (119 events) (Figure 1), alongside local seismic network derived mechanisms

Figure 6. (a) Map and length weighted rose diagrams showing the different orientations of the mapped faults along the rift axis of the Danakil Depression. The faults are color coded by their sub-region. (b) Map showing the dip direction of the faults mapped. Unknown structures are where the dip direction could not be identified or there is no vertical offset at the surface. Major axial volcanic centers shown alongside volcanic cones which are mapped at a 1:40,000 scale. (c) Density map of the structural features mapped along the Danakil Depression rift axis. The study area is gridded into 1 km^2 regions with a search radius of 1 km from the center point of each region. Faults away from the rift axis are marked by red lines and are from Manighetti et al. (2001). (d) Histograms showing the lengths of faults and fractures in each sub-region. Lengths divided into 1 km bins from 0 to 15 km. N = number of structures mapped in each sub-region.

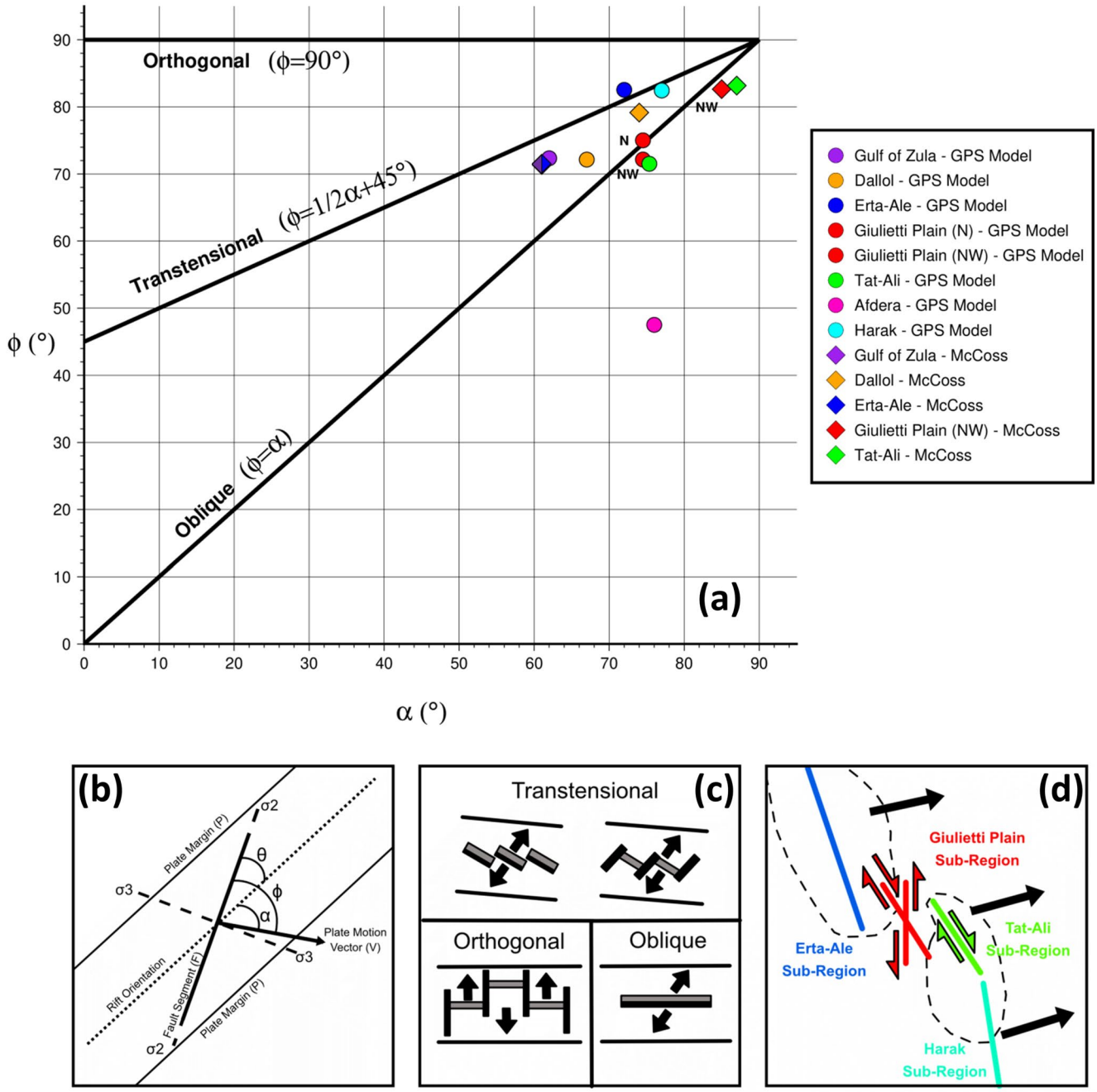

Figure 8. (a) Graph showing the mode of opening occurring in each sub-region of the Danakil Depression based on the methods outlined by Tuckwell et al. (1996). The plate motion vector values are from the GPS model taken from Viltres et al. (2020), shown by circles, or derived by geometrical construction using the methods outlined in McCoss (1986), shown by diamonds. The McCoss values for the Gulf of Zula and Erta-Ale are the same so a split purple/blue diamond is plotted. (b) Angular relationship between the Plate Motion Vector (V), Fault Segment (F) and Plate Margin (P) orientations used to model the mode of opening occurring along the rift axis. (c) Varying modes of extension that are modeled. The gray rift segments indicate where normal opening occurs and the black segments represent strike-slip deformation. A combination of black and gray is used for oblique opening. (d) Illustration of the oblique opening occurring along the Giulietti Plain and Tat-Ali sub-regions due to localized tectonic interaction between the offset Erta-Ale and Harak sub-regions, which are opening transtensionally.

from Illsley-Kemp, Bull, et al. (2018). The focal mechanisms provided insight into the slip style and direction of tectonic deformation occurring along structural features in Afar. Additionally, the T-axis (the minimum compressive stress axis associated with a seismic event) and rake (the direction of fault motion with respect to the strike) values were extracted from focal mechanisms located along the rift axis, thus providing direct constraints on the kinematics of the faulting and enabling a data driven comparison with the kinematics modeling (Figure 8).

4. Results

4.1. Characterization of the Rift Axis Fault Population

Remote sensing methods were used to produce detailed maps of faults and fractures along the rift axis of the Danakil Depression (Figure 6). To characterize the nature of rift axis faulting in each of the sub-regions, various quantitative analyses were conducted, including fault orientation, length and density analysis.

4.1.1. Fault Orientation and Dip Direction

Length-weighted rose diagrams highlight along axis variations in the mean orientation of faults in each sub-region (Figure 6a). Faults in the northern and central sub-regions of the Danakil Depression have a general NNW/SSE trend, with mean orientations of 160° (Gulf of Zula), 155° (Dallol) and 161° (Erta-Ale) (Figure 6a), which are approximately perpendicular to the regional extension direction (NE/SW) (Figure 1). Southwards, a conjugate set of faults orientated approximately N/S (mean orientation of 0°) and NWW/SSE (mean orientation of 147°) is identified across the Giulietti Plain (Figure 6a). Previous mapping of upper crustal features in the step-over zone have also identified this conjugate set of structures with localized tectonic deformation between the offset Erta-Ale and Tat-Ali magmatic segments interpreted as the likely cause (Illsley-Kemp, Bull, et al., 2018; La Rosa et al., 2019). The faults of the Tat-Ali sub-region have a mean orientation of 146° (Figure 6a). However, faulting in the Afdera sub-region differs from the NNW/SSE regional trend with a mean orientation of 26° (Figure 6a). This is likely a result of the Afdera sub-region being part of the step-over zone between the Danakil Depression and the Dabbahu-Manda-Harraro magmatic segment, located en-echelon to the SW (Figure 3). The structural features in the Harak sub-region, the southernmost in the Danakil Depression, have more of a N/S trend with a mean orientation of 171° (Figure 6a).

Most structures dip westwards in the northernmost part of the Depression (Gulf of Zula sub-region) (Figure 6b), with a change to eastward dipping south of the step-over in the rift axis between the Gulf of Zula and Dallol sub-regions (Figure 6b). Southwards, along the Tat-Ali magmatic segment most structures again dip westwards; the faults of the Afdera sub-region dip both E and W (Figure 6b). The Harak sub-region comprises of two sets of structures located either side of an axial graben. On the eastern border of the graben, most structures dip westwards with a few antithetic faults dipping east, whilst the faults bordering the western side of the Depression dip eastwards (Figure 6b). However, moving further west of the western border of the graben in the Harak sub-region, faults tend to start dipping westwards.

4.1.2. Fault Density

The highest fault density values were recorded at the southern and northern ends of the Danakil Depression, with maximum values of 3.9 km/km^2 and 3.2 km/km^2 for the Harak and Gulf of Zula sub-regions (Figure 6c). The tips of the Erta-Ale (maximum value of 2.7 km/km^2 at the southern end) and Tat-Ali (maximum value of 2.6 km/km^2 at the northern end) magmatic segments also have elevated densities in faulting (Figure 6c). Additional regions of elevated fault density include step-over zones between the rift segments, such as the Giulietti Plain (maximum value of 2.65 km/km^2), and the rift step between the Gulf of Zula and Dallol sub-regions (maximum value of 3.2 km/km^2) (Figure 6c). The low fault density in the Dallol sub-region is likely due to numerous structures being obscured by evaporite deposits covering the surface, and is likely underestimated. Localized pockets of higher density values along the Erta-Ale magmatic segment are often located at axial volcanic centers. However, relative to the other sub-regions, Erta-Ale has the lowest fault density potentially related to magmatism accommodating most of the strain along magmatic segments or recent lava flows obscuring faults and fractures. In general, along the rift axis there is a large variation in fault density (0–3.9 km/km^2) which may be the result of varying importance of faulting accommodating the extension.

4.1.3. Fault Length

Histograms of fault lengths in each sub-region (Figure 6d), show lengths between <1 and 15 km, with most faults being <3 km. Mapping structural features visible at a 1:40,000 scale means that the proportion of smaller length structures (e.g., 0–1 km) is likely under estimated. Most sub-regions are dominated by faults of 1–2 km, although the Dallol, Tat-Ali and Afdera sub-regions are exceptions, with the highest frequency bin being 2–3 km for the Dallol and Tat-Ali sub-regions and 0–1 km for Afdera. Afdera and Harak, the southernmost sub-regions, have the largest average fault length values, with both having mean fault lengths of 4.2 km and median length values of 3.7 km (Afdera) and 3.4 km (Harak), respectively. Both of these sub-regions also have the largest range in fault length with several faults 10–15 km long. However, northwards the Gulf of Zula, Erta-Ale, Giulietti Plain

and Tat-Ali sub-regions only have structures <10 km in length, with the majority <5 km. As a result, the average fault lengths for these regions are also lower, with mean lengths 2.4–2.8 km and median lengths 1.9–2.4 km. This analysis shows there is an increase in both the average and range of fault lengths at the southern end of the Danakil Depression when compared with the northern and central parts of the basin.

4.2. Fault Topology

The topological characteristics of the fault networks in each sub-region in the Danakil Depression were analyzed and compared (Figure 7). The relative proportion of I-, Y- and X-nodes for each sub-region are shown in the ternary plot Figure 7b. In general, I-nodes dominate, with all of the sub-regions plotting along the I-Y axis as a result of the low number of X-nodes, with >90% I-nodes for all the sub-regions. The exception is the Harak sub-region (Figure 7b) where a greater proportion of Y-nodes (27%) occur (Figure 7b). Figure 7c shows the proportion of branch types (e.g., I-I, I-C, C-C) for each sub-region, with 3 clusters produced. Erta-Ale and Dallol sub-regions have the highest proportion of I-I branch types (>90%) (Figure 7c). The second group of sub-regions (Gulf of Zula, Giulietti Plain, Tat-Ali and Afdera) have a relatively higher percentage of C-I and C-C branches (Figure 7c), and the Harak sub-region has an even greater amount of C-I and C-C branches (Figure 7c). The contours on the ternary plots show the average number of connections per branch, with Harak having a value of 1.07, which is much greater than the other sub-regions. These ternary plots indicate that the Harak sub-region has a greater connectivity between faults when compared with the other sub-regions to the north.

4.3. Kinematic Analysis

Using the geometrical relationship between the orientation of the structural features in each sub-region (Figure 6a), the tectonic extensional direction and the rift axis azimuth, the current kinematics along the rift axis in the Danakil Depression can be understood using the methods outlined in Tuckwell et al. (1996). This method has been previously employed in magma-rich continental rift settings, including in the East African rift system (Robertson et al., 2016; Siegburg et al., 2020). Plotting the length weighted mean orientations of the structural features (F) from each sub-region and the overall rift trend (P) of 150° against the recent relative plate motion (V), the mode of opening can be classified either as orthogonal, transtensional or oblique. The method outlined in Tuckwell et al. (1996) uses the relationship between α (the angular difference between V and P) and φ (the angular difference between V and F) to indicate the mode of opening occurring (Figure 8).

The relative plate motion values have been taken from a kinematics block model based on GPS measurements, providing the along rift axis opening vectors (V_{gps}) in the Danakil Depression, which decrease southwards from 88° (~14.8°N) to 73° (~13°N) (Figure 3; Viltres et al., 2020). Additionally, we calculated the relative plate motion ($V_{calculated}$) via the geometrical construction of McCoss (1986), using the length weighted average orientation of the mapped faults for the maximum horizontal stress ($S_{hmax} = \sigma_2$) and their perpendicular angle for the minimum horizontal stress ($S_{hmin} = \sigma_3$) (Figure 8). The rift margin was defined as the Danakil Block (143°) for the McCoss (1986) geometrical construction, which borders the eastern margin of the Depression, due to the rotational mode of opening occurring in a NE direction. The calculated plate motion vectors ($V_{calculated}$) range from 63 to 89° (decreasing southwards) along the axis, although values of 130° and 117° were calculated for the N-S conjugate set of structures on the Giulietti Plain and the Harak sub-region. The NE regional opening direction means these values are implausible, and therefore not used.

The Gulf of Zula and Erta-Ale sub-regions both plot along the transtensional opening model when using either $V_{calculated}$ (GZ = 89°, EA = 89°) or V_{gps} (GZ = 88°, EA = 78°) as the relative plate motion values (Figure 8a). The Dallol sub-region also plots along the transtensional model when using the $V_{calculated}$ value (76°) as the relative plate motion (Figure 8a). However, when using V_{gps} (83°) the Dallol sub-region plots more closely to the oblique model (Figure 8a). This variation may be a result of the structural features in the Dallol sub-region largely being inferred. Both the NW/SE and N/S conjugate set of structures identified across the Giulietti Plain sub-region plot as opening in an oblique manner when using V_{gps} (75.5°) as the relative plate motion. The NW/SE set of conjugate structures are also identified as opening in an oblique fashion when using $V_{calculated}$ (65°). Furthermore, the Tat-Ali sub-region also plots along the oblique model using either V_{gps} (74.66°) or $V_{calculated}$ (63°) (Figure 8a). The Afdera sub-region plots significantly beneath the oblique model when using V_{gps} (74°), indicating strike-slip kinematics to be occurring in this area. This supports the hypothesis of these faults representing a linkage zone

between the Danakil Depression and the Dabbahu-Manda-Hararo segment to the SW (e.g., Schaegis et al., 2021). Harak, the southernmost sub-region in the Depression, has been modeled as opening in a transtensional fashion when using V_{gps} (73°) (Figure 8a). The kinematics analysis indicates the mode of opening changes along the rift axis in the Danakil Depression, with most of the basin opening transtensionally but with obliquity increasing southwards.

4.4. Focal Mechanisms and Tectonic Stresses

Focal mechanisms for Afar earthquakes from Illsley-Kemp, Bull, et al. (2018) and the Global CMT catalog are shown in Figure 9b. Five focal mechanisms from the Global CMT catalog (blue) are located along or near the rift axis in the Danakil Depression. In the Dallol region, focal mechanisms 050693E (5.2 M_L), 102204D (5.4 M_L) and 200604101336A (4.9 M_L) indicate normal slip deformation (Figure 9b). In contrast, focal mechanisms 200710020906A and 201906301426A are located on the Giulietti Plain and are from strike-slip/oblique slip earthquakes of 5 and 4.9 M_L (Figure 9b). Additional focal mechanisms (red) on the Giulietti Plain are from Illsley-Kemp, Bull, et al. (2018) but are from much smaller magnitude earthquakes (<2 M_L) (Figure 9b).

Extracting the T-axis and rake values of the focal mechanisms helps to understand the kinematics along the rift axis. The T-axis azimuth from the northernmost Global CMT focal mechanisms is ~70°/250°; on the Giulietti Plain it is ~60°/240° (Figure 9a). Focal mechanism's 050693E, 102204D and 200604101336A, located in the Dallol sub-region, have rake values that indicate normal fault slip (approx. −90°) (Figure 9c). Southwards at the Giulietti Plain, the Global CMT focal mechanisms (201906301426A, 200710020906A) have rake values that plot along the sinistral strike-slip deformation (approx. 0°) (Figure 9c). However, the rake values from Illsley-Kemp, Bull, et al. (2018) focal mechanisms indicate dextral strike-slip deformation (approx. 180° or −180°) (Figure 9c). Therefore, the variability of focal mechanisms is consistent with the structurally interpreted conjugate set of strike-slip/oblique slip faults across the Giulietti Plain.

4.5. Subsurface Structural Interpretation From Seismic Reflection Data

Linking LINE-7 and LINE-8 (sub-parallel in orientation) (Figure 10a) provides a full across-strike profile of the rift axis, including both eastern and western margins (Figure 4), therefore these lines are the main focus of our results and interpretation. The reflections in the Overburden unit (above Horizon A) are mostly sub-parallel in nature, with the URS (between Horizons A and B) and Bischofite (between Horizons B and C) units also showing sub-parallel reflections in the central part of the basin. However, toward the western and eastern margins, the URS and Bischofite reflections become tilted, likely due to faulting. Horizon A is a strong continuous reflection, with the reflectors above this horizon broadly continuous but showing lateral variation in amplitude. Beneath Horizon A, the reflections are continuous with strong amplitudes in the central and eastern parts of the central basin. However, toward the western rift margin, these reflections become more discontinuous with sections of low amplitude reflectors, perhaps a result of the numerous faults present along the western margin of the basin. Beneath Horizon C, reflectors are discontinuous in nature, and are weak in many of the seismic lines, thus making interpretation of deeper structures challenging.

A 10 km wide asymmetrical basin, bounded by faults 7.1 and 7.12 (from 801 to 4801), is present across LINE-7 with significant subsidence in the central part of the rift axis (Figure 10a). LINE-7 shows 4 major E-dipping faults on the western side of the rift axis (7.1, 7.3, 7.4 and 7.8), likely striking NW (Figure 4), that extend from 500 ms TWT to just below the surface (Figure 10a). Despite being a major structure, fault 7.1 has a throw of just 27 ± 3 m for Horizon B, compared with faults 7.3, 7.4 and 7.8 which have throws of 55 ± 5 m, 118 ± 10 m and 85 ± 5 m for Horizon B, respectively (Figure 10). The throw of faults 7.3 and 7.4 appear to increase with depth (Figure 10). Numerous minor faults are also observed on the western side of the rift, with some structures antithetic in nature, dipping W (Figure 10). On the eastern side of the rift axis, there are 4 W-dipping major faults accommodating extension, with no minor faulting (Figure 10). With no other parallel seismic lines extending to the eastern margin of the rift axis, the strike of these faults cannot be determined. Faults 7.10, 7.11 and 7.12 extend from 1,000 ms TWT to close to the surface and have significant throw, fault 7.10 has 74 ± 8 m vertical displacement for Horizon B (Figure 10). Fault 7.13 is only mapped as deep as 500 ms TWT and does not reach the Overburden unit, and also has a comparatively reduced throw of 34 ± 3 m (Figure 10). LINE-8 has two W-dipping faults but they appear to be minor structures (Figure 10). Comparing the faults identified in seismic reflection data with those inferred from the remote sensing mapping in the Dallol sub-region, shows that the

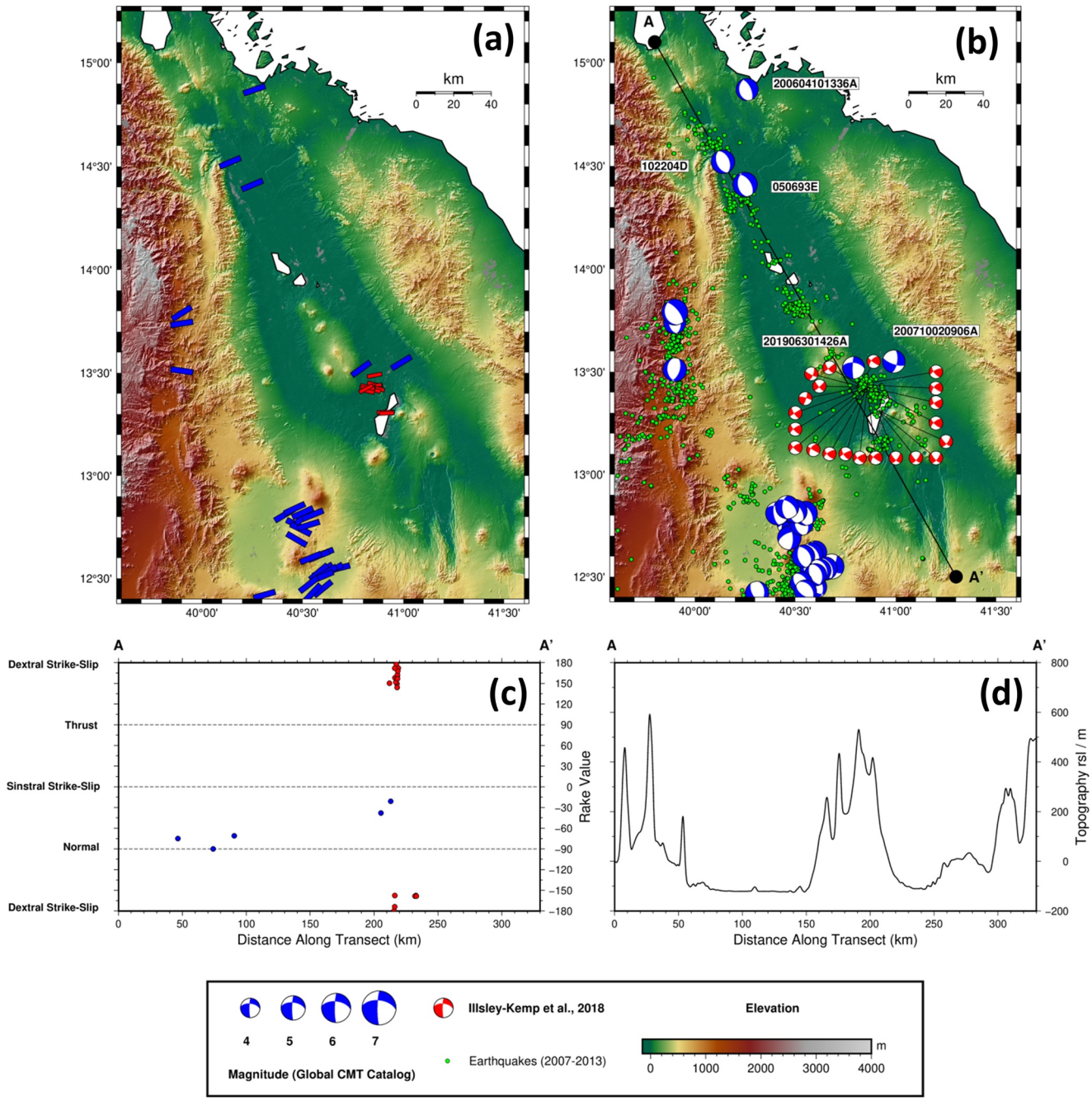

Figure 9. (a) T-axis values extracted from focal mechanisms in the Danakil Depression. (b) Focal mechanisms from Global CMT catalog (blue focal mechanisms) and Illsley-Kemp, Bull, et al. (2018) (red focal mechanisms) plotted. (c) Rake values extracted from focal mechanisms along the rift axis transect (A-A') showing the mode of opening occurring and changing along the rift axis. (d) Topography along A-A' transect.

major faults on the margins of the rift axis are often visible as linear features at the surface (Figures 4, 6a, 10a). This is due to these marginal major faults often extending close to the surface, however the minor faults in the center of the graben are thickly buried by evaporites and thus do not show any surface feature (Figures 4 and 10a). This indicates that despite the remote sensing mapping of the faults in the Dallol sub-region being incomplete, the major faults were still identified.

Horizon C (base of the Bischofite) reaches 500 ms TWT in the hanging wall of Fault 7.10, indicating significant subsidence related to fault activity (Figure 10a). The sedimentary units between Horizons A-C (URS and Bischofite) show the same trends in lateral thickness variation across the rift basin, with the units being thickest

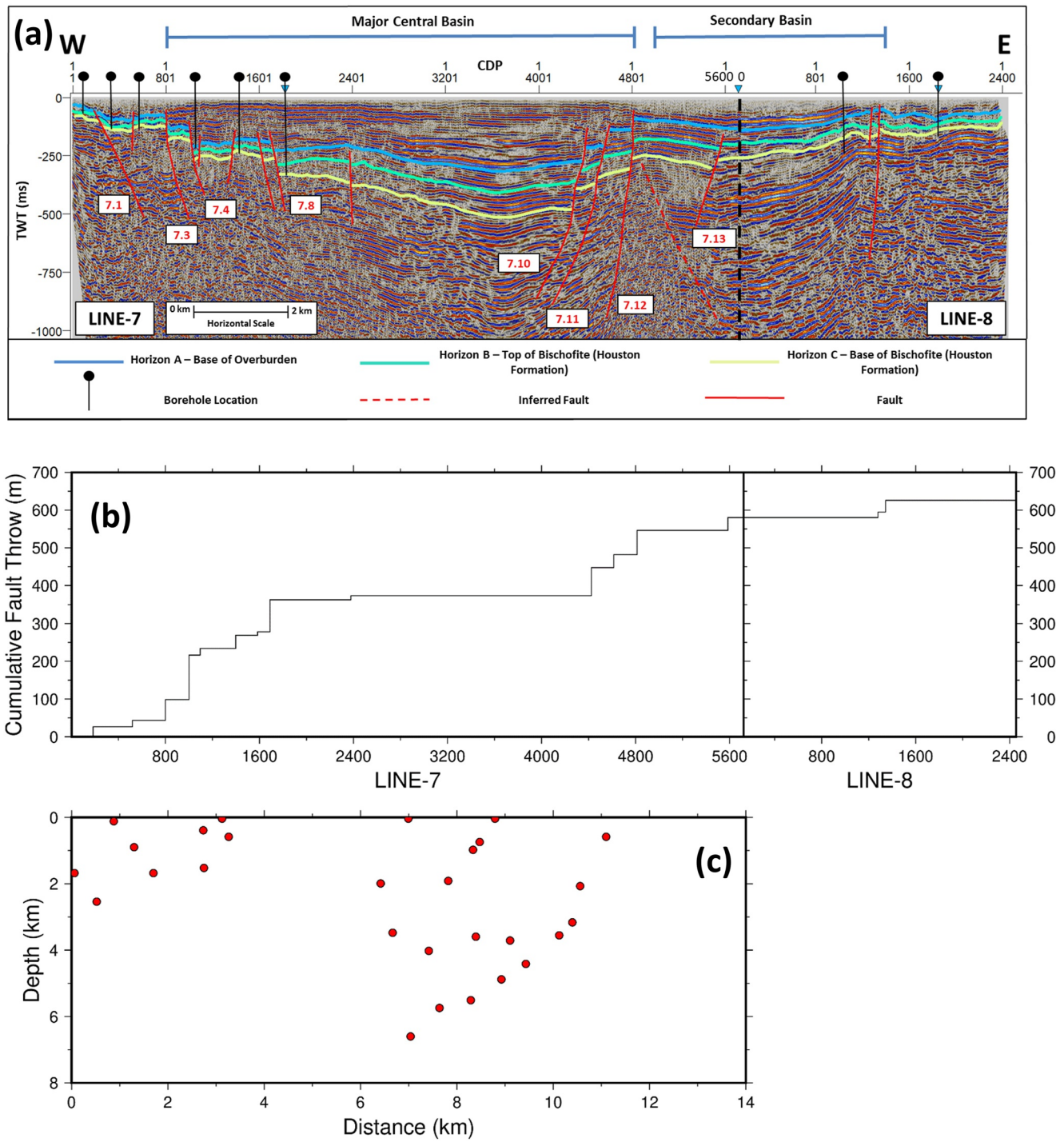

Figure 10. (a) Interpreted E-W seismic lines LINE-7 and LINE-8 overlain by mapped Horizons A-C and identified faults, showing the rift axis structure in the Dallol sub-region. The individual faults mentioned in the text are labeled by the boxed red numbers. (b) Cumulative fault throw along the across rift-axis seismic profile. (c) Earthquake locations along LINE-7 from projecting events onto the Earthquake Axis Profile (Figure 4) from 1.5 km N and S of the profile. Earthquake locations reflect the asymmetrical structure of the major central basin in the Dallol sub-region identified in the seismic reflection data (a).

in the central part of the rift as a result of slip along the major faults on the eastern side of the basin (e.g., 7.10) (Figure 10a). Since 100 ka (assumed age of Horizon B), 600 ± 25 m of sediment (calculated using Overburden and URS velocity values from Lascialfari, 2017) has been deposited in the main central basin. The URS and Bischofite units start (from 1800 LINE-7) to thin out toward the western margin of the central basin (Figure 10a).

Table 1
Cumulative Fault Extension and Slip Rates Across the Rift Axis (LINE-7 and LINE-8)

	Across axis section	Cumulative throw (m)	Fault dip	Cumulative extension (m)	Cumulative fault slip (m)	Cumulative extension rate (mm/yr)	Cumulative slip rate (mm/yr)
Maximum rate values	West	400	50	336	522	3.4	5.2
	East	270	50	213	352	2.1	3.5
	Total	670	50	549	874	5.5	8.7
Median rate values	West	374	60	216	432	2.2	4.3
	East	252	60	146	291	1.4	2.9
	Total	626	60	362	723	3.6	7.2
Minimum rate values	West	345	70	125	367	1.2	3.7
	East	235	70	95	250	1	2.5
	Total	580	70	220	617	2.2	6.2

Note. Maximum, median and minimum throw values calculated from the seismic reflection interpretation and lithological velocities (Lascialfari, 2017) along with a range of dip values 50–70° used to calculate extension and slip across faults. The 100 ka age for Horizon B is used to calculate the median as well as maximum and minimum cumulative extension and slip rates for across the rift axis in the Dallol sub-region.

However, along LINE-8 and the eastern end of LINE-7 these units are a consistent thickness until thinning out at the eastern end of LINE-8 (Figure 10a). Deeper reflectors (>500 ms) along LINE-8 and the eastern end of LINE-7 indicate the presence of a secondary basin that is ~5 km wide (from 5000 LINE-7 to 1300 LINE-8) (Figure 10a). An E-dipping antithetic fault has been inferred to border the western margin of this secondary basin (5000 LINE-7) (Figure 10a). Using our current interpretation of the three horizons, recent subsidence of the secondary basin is less than in the major central asymmetrical basin. However, the steeply dipping nature of the deeper reflectors suggests significant subsidence occurred within this secondary basin prior to the deposition of the mapped horizons. This indicates that there have been lateral changes over time in the locus of subsidence across the rift axis. LINES -1 to -5 (Figure 4) show that some faults mapped along the western margin of the rift axis continue northwards of LINE-7 (Figure 4). Fault 7.1 appears to be the western border fault to the central rift axis basin, extending >7 km from LINE-7 to LINE-5 and -4 (Figure 4), possibly linking to the border structure identified along LINE-1 and -2 (Figure 4). Satellite imagery appears to show the surface sediments along the western margin following the trend of this western border fault (Figure 4). Most of faults on LINE's 1 to 5 are extensional in nature, however along LINE-1, two minor reverse faults were identified (Figure 4).

Using the calculated throw values of the 100 ka Horizon B and velocity values for the Overburden and URS units (Lascialfari, 2017), fault slip and extension rates were calculated for all the identified faults mapped along LINE-7 and -8 (Table 1). Fault 7.4, located on the western side of the central basin, has a median (calculated using the median throw and fault dip values) slip rate of 1.4 mm/yr (range of 1.1–1.7 mm/yr), while on the eastern rift, fault 7.10 has median slip rate of 0.85 mm/yr (range of 0.7–1.1 mm/yr). The total sum of the median extension and slip rates for faults along LINE-7 and -8 are 3.6 mm/yr and 7.2 mm/yr, respectively (Table 1). The faults on the western margin (faults 7.1–7.9) have a total extension rate of 2.2 mm/yr and slip rate of 4.3 mm/yr, whereas the faults on the eastern margin (faults 7.10–7.13 and 8.1–8.2) have total extension of 1.4 mm/yr and summed slip rate values of 2.9 mm/yr. Therefore, the faults on the western margin accommodate slightly more extension than faults on the eastern margin.

Some earthquakes from the regional seismic catalog (Belachew et al., 2011; Illsley-Kemp, Keir, et al., 2018) have occurred in the Dallol sub-region. The spatial pattern of this seismicity supports the structural interpretation of a major asymmetrical basin as identified in the seismic reflection data from the Dallol sub-region (Figure 10). The major westward dipping structures on the eastern margin of the major central basin are shown to be seismically active down to 7 km depth (Figure 10c). The faults on the western margin of the basin are shown to be shallower with active seismicity only in the upper 3 km (Figure 10c).

5. Discussion

5.1. Variation in Fault Characteristics Along the Danakil Depression Rift Axis

Analysis of faulting along the rift axis in the Danakil Depression highlights an increase in faulting in the north and south of the rift relative to its the center, where the Erta-Ale and Tat-Ali magmatic segments are located. There is also a distinctive change in fault character at the southern end of the Danakil Depression, compared to the center and north. This change is especially evident in the Harak sub-region, which has a higher fault density, longer faults (>10 km), a larger range of fault lengths, and increased fault connectivity relative to the other sub-regions (Figures 6 and 7). The neighboring Afdera sub-region, west of Harak, also has a longer average fault length than the central and northern sub-regions (Figure 6d).

Several factors may cause these variations in faulting along axis. A primary control on fault scaling is elastic thickness (e.g., Ebinger et al., 1999; Jackson & White, 1989;

Scholz & Contreras, 1998), which can be modulated by crustal thickness, heat flow and pre-existing weaknesses (e.g., Burov & Diament, 1995; McKenzie et al., 2005; Tesauro et al., 2012). In the Danakil Depression, crustal thickness increases at the southern end of the basin (Figure 2) and offers one explanation for the increased fault lengths in the Harak and Afdera sub-regions (Figure 6d). Elevated heat flow from localized magmatism can reduce the thickness of the elastic layer resulting in shorter faults (Dumont et al., 2017). The Harak sub-region is distinctive in that it is within 3.5–0.6 Ma Stratoid volcanic rocks, and lacks the Holocene volcanism common in the other sub-regions (Beyene & Abdelsalam, 2005). Stronger crust due to a lack of recent magmatism may therefore contribute to facilitating longer faults in the Harak sub-region.

Increased fault length and connectivity in the Harak sub-region (Figures 6d and 7), in the southern rift, compared with sub-regions further north indicate a more evolved fault network (Cowie et al., 2005; Gawthorpe & Leeder, 2000). The formation of the Erta-Ale and Tat-Ali magmatic segments in the central part of the Danakil Depression has resulted in large amounts of surface magmatism during the Holocene (Bastow & Keir, 2011; Keir et al., 2013). This magmatism may also cover/mask a more evolved fault network present at depth, making it appear less connected and less mature at the surface. The older surface lithology (3.5–0.6 Ma) in the Harak sub-region (Beyene & Abdelsalam, 2005) and the lack of recent volcanism may lead to the mature fault network being visible at the surface. Varying surface magmatism along the rift axis may therefore contribute toward the observed surface structure.

Variations in fault characteristics are more subtle in the northern and central part of the rift than the southern. Fault density is the characteristic that differs most (Figure 6c), with very few faults identified in the central Erta-Ale sub-region relative to the Gulf of Zula and Dallol sub-regions further north (and relative to the southern rift). The Danakil Depression therefore shows an increase in fault density toward the northern and southern rift tips (Figure 6c). The faulting style along slow spreading mid-ocean ridge segments shows a similar spatial variation (Carbotte et al., 2016), with higher displacement faults toward the segment tips (e.g., Escartin et al., 1999; Shaw, 1992; Shaw & Lin, 1993). These variations support the hypothesis of along-axis variations in contribution of faulting to extension relative to magmatism, with increased importance of faulting (and reduced magmatism) toward segment tips. We suggest that a similar mechanism may be applicable to the Danakil Depression. Similar spatial relationships have also been observed along magmatic segments in the Main Ethiopian Rift (Gedemsa, Boset, Kone and Fantale segments) (Kurz et al., 2007; Siegburg et al., 2020). Increased fault densities are also present at step-over zones between en-echelon magmatic segments (Figure 6c), thus faulting is accommodating the transfer of deformation from one segment to another here.

We note that fault characteristics (fault density, length etc.) vary over relatively short distances (10s km) along the rift axis of the Danakil Depression. Although some of these variations may be a function of surface properties and not a true reflection of subsurface structure, much of the variation can be linked to crustal/lithospheric properties, degree of magmatism, and position within the rift segment.

5.2. Variation in Rift Axis Morphology and Structure Along the Danakil Depression Rift Axis

Rift morphology also varies along the axis with axial highs formed by the volcanic ranges of Erta-Ale and Tat-Ali magmatic segments in the central rift (Figures 2, 3 and 11). In contrast, at the northern and southern ends of the rift, axial grabens are present, for example, in the Dallol and Harak sub-regions (see also Bastow et al., 2018) (Figures 2, 3, 10 and 11). The rift axis morphology, like the fault density, appears to be linked with whether the dominant mechanism accommodating extension is magmatism (axial high) or faulting (axial graben). Seismicity data supports magmatism being dominant in the Erta-Ale magmatic segment, with most seismicity in the Erta-Ale sub-region being low frequency in nature (Illsley-Kemp, Keir, et al., 2018). In contrast, high frequency earthquakes, attributed to mechanical deformation, occur along sections with reduced magmatism, such as the Dallol sub-region (Illsley-Kemp, Keir, et al., 2018).

At oceanic spreading ridges, across axis topographic variations are also observed and thought to be closely linked to magma supply (Liu & Buck, 2020; Phipps Morgan & Chen, 1993). For example, ≤500 m axial highs are observed where magma supply is elevated, such as the segment centers of slow spreading ridges (Liu & Buck, 2018; Phipps Morgan & Chen, 1993). In contrast, lower and episodic magma supply, is associated with ≤2 km deep axial grabens (Liu & Buck, 2018; Phipps Morgan & Chen, 1993). Therefore, we interpret the origin of the morphological variations for the Danakil Depression to be along-rift variations in magma supply similar to that observed at ocean spreading centers.

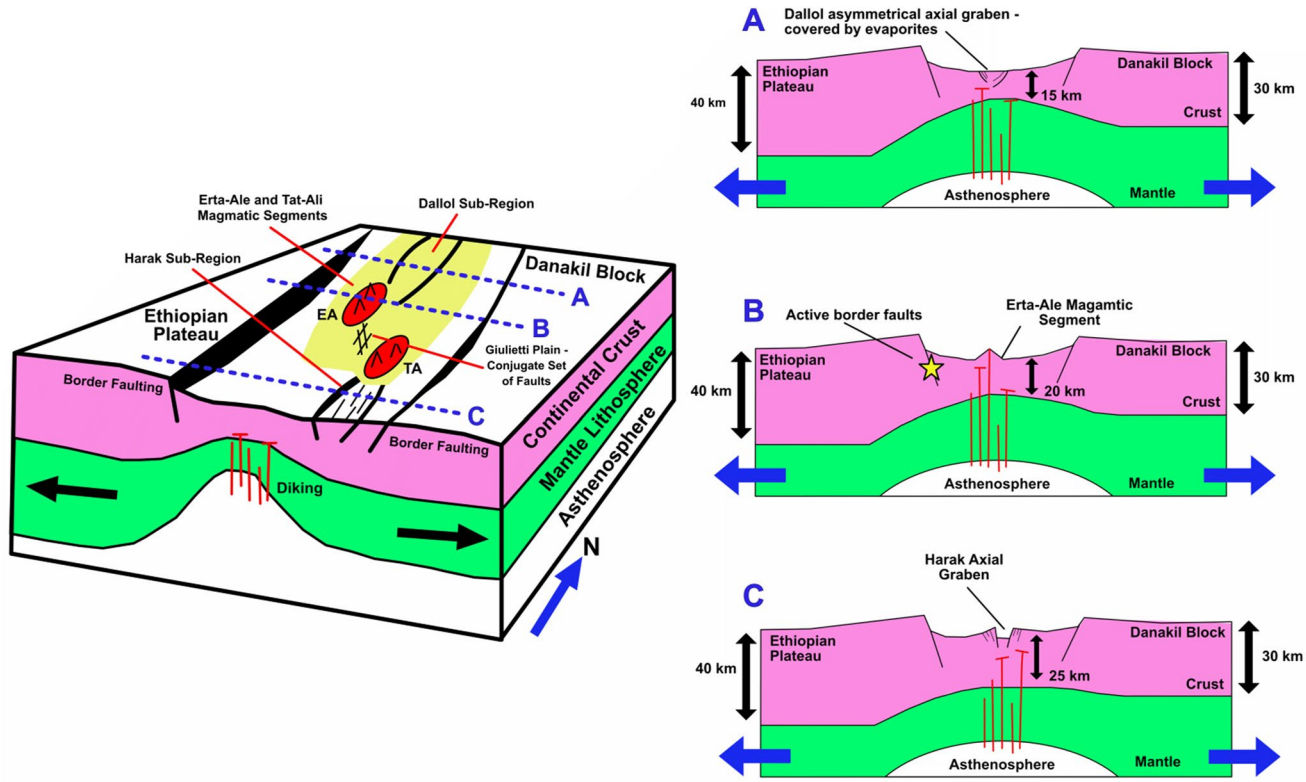

Figure 11. Structural synthesis of the Danakil Depression describing the spatial relationship between the Erta-Ale (EA) and Tat-Ali (TA) magmatic segments, and the axial grabens (e.g., Dallol and Harak) along the rift axis. 2D profiles A–C show the morphology changes along the rift axis caused by the mechanisms accommodating extension, with axial highs in magma-rich areas but axial grabens in magma-poor sub-regions.

Along oceanic spreading centers, crustal thickness is often greatest at the center of spreading segments and reduced at the segment tips (e.g., Canales et al., 2000; Detrick et al., 1995; Hooft et al., 2000; Kuo & Forsyth, 1988). In the Danakil Depression however, this spatial relationship is not observed, with crustal thickness thinning from 25 km at the southern end of the basin to 15–20 km beneath the Erta-Ale magmatic segment, and then continuing to thin northwards toward the Dallol sub-region (Figures 2 and 11). In addition, the seismic velocity structure of the crust beneath the Danakil Depression indicates that it is heavily intruded continental crust and not yet oceanic crust (Hammond et al., 2011; Makris & Ginzburg, 1987). This contrast in crust type and along rift thickness variations compared to ocean ridges, but similar rift morphology, supports the interpretation that the rift axis morphology (graben or axial high) is independent of crustal structure. Therefore, the rift morphology of evolved continental rifts can mimic that of ocean ridges if magma supply processes and mechanisms of extension are similar. Our observations subsequently also suggest that axial morphology and its along-rift variations could initiate during late-stage continental rifting when the broad scale and deeper lithospheric structure is still that of a continental rift.

Toward the north of the Danakil Depression, sedimentary cover obscures the surface fault network, but seismic reflection data places constraints on rift structure. Seismic reflection data from the Dallol sub-region show the major central basin of the rift to be asymmetrical with eastern margin faults dominant. On the eastern margin, there are a few major faults and very few minor structures, but extension on the western margin is distributed across numerous minor faults alongside a few major faults (e.g., fault 7.4) (Figure 10). Bastow et al. (2018) identified a major fault on the western margin from seismic lines ~15 km further south in the Dallol sub-region, which has a throw of ≤400 m across the top of the Houston Formation (Horizon B) and a slip rate of 3.8–5 mm/yr over the last 100–120 Kyr. These slip rate and throw values are far greater than any calculated for the individual faults identified in this study on the western margin of the major central basin (or any other individual structure identified on the eastern margin of LINE-7 and LINE-8). Therefore, the structure and mechanism of accommodation of extension along the western margin of the Dallol axial graben appears to change from a singular dominant

major fault to numerous faults over a distance of just 15 km in the Dallol sub-region. Additionally, there is a switch in polarity of the major central basin structure, from the major faults on the eastern side of the basin being dominant as shown by this study, to the major fault on the western margin being dominant 15 km south (Bastow et al., 2018), as indicated by the dip direction of the basin sedimentary sequences. We also note that the maximum depth of Horizon B below the surface increases slightly from ~600 m in the major central basin (LINE-7 and -8) to ~740 m further south (Bastow et al., 2018), suggesting a persistent central graben but with increased subsidence southwards over the last ~100 ka. The seismic lines located northwards (LINE-1 to -5, see Figure 4) of LINE- 7 and -8 show the western margin of the rift axis, with the interpreted horizons also dipping eastwards, indicating that the central graben continues further north. The lack of subsurface information regarding the axial graben in the Harak and Gulf of Zula sub-regions makes comparing the axial structure in these areas with the Dallol sub-region challenging. Our remote sensing analysis shows that the faults on both the E and W margins of the graben in the Harak sub-region dip toward the axis (Figure 6b). However, most faults mapped in the Gulf of Zula sub-region dip westwards (Figure 6b), possibly a result of it being a one of the marginal grabens with antithetic faulting located along the base of the Ethiopian Plateau (Zwaan, Corti, Sani, et al., 2020).

There are clear changes in morphology along the Danakil Depression rift axis related to the likely dominant extensional mechanism (faulting or magmatism), with a synthesis of the faulting and magmatic processes occurring in the Danakil Depression and their spatial relationship shown in Figure 11. However, there are also variations in the structure of the axial graben between different sections of the rift axis where upper crustal faulting likely dominates (e.g., northern and southern parts of the Dallol sub-region), over relatively short distances, with apparent changes in polarity.

5.3. Variation in Rift Opening Style of the Danakil Depression

Kinematic modeling (Figure 8) indicates a transition from transtensional opening in the northern and central sections of the rift to oblique opening in the south (Giulietti Plain and Tat-Ali sub-regions). Analysis of the earthquake focal mechanisms supports this modeling, with rake values in the Dallol sub-region, located in the north, indicating normal fault slip (Figure 9). This changes southwards to dextral and sinistral strike-slip components in the Giulietti Plain (between the central Erta-Ale and Tat-Ali magmatic segments) (Figure 9).

The conjugate set of structures (N-S and NW-SE) across the Giulietti Plain (Figure 6a) are interpreted to be the result of localized extension due to interaction between the en-echelon Erta-Ale and Tat-Ali magmatic segments. Previous studies here have also identified oblique deformation with both sinistral and dextral strike-slip faulting present (La Rosa et al., 2019, 2021). The rake values show that the larger magnitude earthquakes in the Global CMT catalog are related to sinistral deformation and the lower magnitude earthquakes (Illsley-Kemp, Bull, et al., 2018) are dextral in nature (Figure 9). Structural data and InSAR modeling by La Rosa et al. (2019) support these findings, with strain being primarily accommodated by sinistral oblique slip along the N-S trending set of conjugate structures. The dextral oblique slip is accommodated by a secondary NW-SE trending conjugate set of faults, making a relatively minor contribution to strain accommodation (La Rosa et al., 2019).

Our analysis also shows that the faults in the Tat-Ali sub-region have the same orientation as the NW-SE set of structures mapped across the Giulietti Plain, differing from the Harak sub-region to the south (Figure 6). From this, as well as the configuration of the rift axis and the apparent anti-clockwise change in orientation of the northern end of the Tat-Ali magmatic segment (Figure 8d), we interpret the oblique opening in both the Giulietti Plain and Tat-Ali sub-regions to be a result of the lateral step in the rift axis from the Erta-Ale to Harak sub-regions. Therefore, the oblique extension in the Danakil Depression is caused locally by segmentation along the rift axis.

An alternative explanation for oblique extension is magmatic intrusion along the rift axis. Dykes can open pre-existing or new faults when the fluid pressure P_f (fluid = magma) is greater than the minimum compressive stress of the regional stress field (Delaney et al., 1986; Jolly & Sanderson, 1997), with the intrusion of the dyke likely to be perpendicular to σ_3. However, if $P_f > \sigma_2$ then the opening of fractures with any orientation can occur; if $\sigma_3 < P_f < \sigma_2$, then a limited range of fault orientations can open (Jolly & Sanderson, 1997). Therefore, if the fluid pressure of the magmatism is sufficient, faulting with a greater obliquity can occur. However, we interpret that magmatism is not causing the oblique opening in the Danakil Depression, since there is no observed along axis correlation between degree of magmatism and rift kinematics. Magma-rich and magma-poor conditions are observed for sections of the rift axis opening both transtensionally and obliquely.

A final hypothesis to explain oblique extension would be pre-existing structures or reactivation of existing faults along the rift axis. Existing structures from earlier stages of rift development orientated obliquely to the extension direction may be easier to reactivate than the formation of new faults orthogonal to the T-Axis of minimum compressive stress. This was observed near the Bárðarbunga caldera in Iceland where, during the 2014–2015 eruption, pre-existing fractures from earlier rifting were reactivated resulting in oblique opening (Ruch et al., 2016). However, the presence of oblique slip on two fault sets (N-S and NW-SE orientated) in regions experiencing oblique opening points toward their origin not being pre-existing structures.

Non-orthogonal deformation along a rift axis due to segmentation is common in many rift settings and not unique to the Danakil Depression. However, there are a variety of different models that have been shown to accommodate extension in en-echelon zones of deformation. In Iceland, the bookshelf faulting model has been proposed as the mechanism accommodating shear motion in step-over zones, with strike-slip extension sub-parallel to magmatic segments (Einarsson, 2008; Green et al., 2014). This differs from the Giulietti Plain, where the deformation is oblique in nature. Elsewhere in East Africa, linkage between the Red Sea and Gulf of Aden rifts in Central Afar occurs through rift-perpendicular shearing at segment tips across a distributed deformation zone (Pagli et al., 2018), thus also differing from the Giulietti Plain. Along ocean spreading centers, transform faulting links en-echelon axial segments in the form of ridge-perpendicular pure strike-strike slip deformation occurring (MacDonald et al., 1988). The oblique deformation occurring across the Giulietti Plain and Tat-Ali sub-region may represent a proto-transform fault (Illsley-Kemp, Bull, et al., 2018), therefore another indication of the Danakil Depression transitioning to an oceanic spreading center.

5.4. Fault Versus Magmatic Processes Accommodating Extension

The spatial relationship between axial faulting and magmatism supports the hypothesis that extension is primarily accommodated by magmatism within the center of the Danakil Depression but that faulting is more significant toward the ends of the rift. Increasing fault density, length and connectivity away from the magmatic segments suggests that faulting accommodates greater amounts of extension away from the magmatic segments. Additionally, variations in rift morphology correlate with these changes in the relative contribution of faulting and magmatic intrusions, further supporting changes in the primary mechanisms accommodating extension in the upper crust.

Summing the extension rates of the individual faults identified across seismic LINE-7 and LINE-8 (3.6 mm/yr) (Table 1) and then comparing with the GPS-derived extension rate in the Dallol sub-region of $\sim 11.5 \pm 0.5$ mm/yr (Viltres et al., 2020), shows that ~30% of total extension in the upper crust is accommodated by axial faulting. Bastow et al. (2018) estimated an extension rate of 2–3 mm/yr for the major fault controlling the western rift margin, but this value does not account for eastern margin faults or minor structures. Our cumulative extension rate of 3.6 mm/yr (Table 1) is greater than the extension rate calculated by Bastow et al. (2018) but encompasses both rift margins as well as the minor faults. In our study, there are still likely additional faults not imaged or identified in the seismic profiles (e.g., Reston, 2009), as well as active faulting present east and west of the seismic lines (particularly to the east as the lines do not extend fully across the rift basin; Figure 4), thus our extension rate will be an underestimate. Even considering this underestimation, this result indicates significant fault-controlled extension in the parts of the rift where magmatism is reduced, highlighting the importance of faulting in the final stages of break-up even in magma-rich continental rifts. Rift axis faulting also appears to largely accommodate the extension between the offset magmatic segments (e.g., Giulietti Plain, Afdera sub-region).

6. Conclusions

We use mapping of remote sensing data for quantitative analysis of fault characteristics (orientation, length, connectivity and density) along the rift axis of the Danakil Depression, along with interpretation of seismic reflection and borehole data from a magma-poor area of the rift (Dallol sub-region). The analysis of these various datasets, alongside seismicity and geodetic data, provides better understanding of the along-rift variations in mechanism and kinematics of extension in the final stages of continental break-up, and quantitative constraints on rift geometry and the contribution of faulting to extension. We map 586 faults, which increase in density away from the center of magmatic segments, often accompanied by increased fault length and connectivity (e.g., the Harak sub-region in the southern rift). There are changes in rift axis morphology related to the dominant

extensional mechanism, with axial highs along sections of elevated magmatism and axial graben in regions of reduced magmatism (Figure 11). Interpretation of the seismic reflection profiles shows that upper crustal axial faulting in the Dallol sub-region (magma-poor) accommodates 3.6 mm/yr of extension, which comprises ~30% of the total extension (and likely an underestimate), highlighting the importance of faulting even in magma-rich continental rifts. Kinematic modeling and earthquake focal mechanism analysis show the northern and central part of the rift is opening transtensionally but switches to oblique opening across the Giulietti Plain and Tat-Ali sub-regions further south. This obliquity is caused by a lateral step in the rift axis from the Erta-Ale magmatic segment to the Harak sub-region, resulting in localized oblique deformation between rift segments. The spatial relationship between axial faulting and morphology relative to the magmatic segments shows similarities to seafloor spreading centers. Therefore, we propose that the locus and style of crustal extension of oceanic ridge segments initiate during late stage continental rifting. From our observations we have shown that faulting still plays an important role in the final stages of continental break-up despite the increased importance of magmatism.

Data Availability Statement

The faults mapped in this study can be downloaded as a KMZ file from the supplementary information available with this publication. The National Earthquake Information Centre (NEIC) catalogue was sourced from (https://earthquake.usgs.gov/) and last accessed on 03/12/2021. The local seismicity catalogs were sourced from the studies of Belachew et al. (2011) and Illsley-Kemp, Keir, et al. (2018), with the catalogues available in an Open Access GFZ Data Publication (Zwaan, Corti, Keir, et al., 2020) available at http://doi.org/10.5880/fidgeo.2020.017. Earthquake focal mechanism data used in this study were taken from Global Centroid Moment (gCMT) catalog (https://www.globalcmt.org/) as well as the Illsley-Kemp, Bull, et al. (2018) study. Crustal thickness data from the Afar region used in this study is taken from the data tables of the receiver function studies of Ahmed et al. (2022) and Hammond et al. (2011), and also transposed directly from the wide-angle seismic profiles of Makris and Ginzburg (1987). Regional gravity collated for this study is taken from Figure 2.10 of Bedada (2010), with the thesis available at https://era.ed.ac.uk/handle/1842/4726 and from Figure 3 of Tiberi et al. (2005). GPS data from the Afar region is attributed to McCluskey et al. (2010) and Viltres et al. (2020). The Multispectral Landsat satellite imagery used for remote sensing mapping was sourced from the USGS Earth Explorer (https://earthexplorer.usgs.gov). Topological and geometric analysis of the fault network mapped was conducted using the NetworkGT toolbox (Version 0.0.1) (Nyberg et al., 2018) which is available at https://doi.org/10.1130/GES01595.S1. Maps created using Generic Mapping Tools (GMT) version 6 (Wessel et al., 2019a, 2019b), available at https://www.generic-mapping-tools.org/.

Acknowledgments
GH acknowledges support from PhD studentship funded by the Natural Environmental Research Council (Grant NE/S007210/1). DK was supported by NERC Grant NE/L002531/1 and Italian MIUR PRIN project 2017P9AT72. We thank Quality Seismic Consultancy Limited for provision of the seismic reflection and borehole data.

References

Acocella, V. (2006). Regional and local tectonics at Erta Ale caldera, Afar (Ethiopia). *Journal of Structural Geology*, *28*(10), 1808–1820. https://doi.org/10.1016/j.jsg.2006.06.014

Ahmed, A., Doubre, C., Leroy, S., Keir, D., Pagli, C., Hammond, J. O. S., et al. (2022). Across and along-strike crustal structure variations of the Western Afar margin and adjacent plateau: Insights from receiver functions analysis. *Journal of African Earth Sciences*, *192*, 104570. https://doi.org/10.1016/j.jafrearsci.2022.104570

Anderson, E. M. (1951). *The dynamics of faulting and dike formation with application to Britain* (2nd ed.). Oliver and Boyd.

ArRajehi, A., McCluskey, S., Reilinger, R., Daoud, M., Alchalbi, A., Egintav, S., et al. (2010). Geodetic constraints on present-day motion of the Arabian Plate: Implications for Red Sea and Gulf of Aden rifting. *Tectonics*, *29*(3), TC301. https://doi.org/10.1029/2009TC002482

Autin, J., Leroy, S., Beslier, M.-O., D'Acremont, E., Razin, P., Ribodetti, A., et al. (2010). Continental break-up history of a deep magma-poor margin based on seismic reflection data (northeastern Gulf of Aden margin, offshore Oman). *Geophysical Journal International*, *180*(2), 501–519. https://doi.org/10.1111/j.1365-246X.2009.04424.x

Ayalew, D., Ebinger, C., Bourdon, E., Wolfenden, E., Yirgu, G., & Grassineau, N. (2006). Temporal compositional variation of syn-rift rhyolites along the western margin of the southern Red Sea and northern Main Ethiopian Rift. *Geological Society, London, Special Publications*, *259*(1), 121–130. https://doi.org/10.1144/GSL.SP.2006.259.01.10

Barberi, F. (1971). *Carte Geologique de la Depression Des Danakil (Afar Septentrional - Ethiopie)*. Centre national de la recherche scientifique.

Barberi, F., & Varet, J. (1970). The Erta-Ale volcanic range (Danakil Depression, northern Afar, Ethiopia). *Bulletin Volcanologique*, *34*(4), 848–917. https://doi.org/10.1007/BF02596805

Barberi, F., & Varet, J. (1977). Volcanism of Afar: Small-scale plate tectonics implications. *The Geological Society of America Bulletin*, *88*(9), 1251–1266. https://doi.org/10.1130/0016-7606(1977)88<1251:VOASPT>2.0.CO;2

Bastow, I. D., Booth, A. D., Corti, G., Keir, D., Magee, C., Jackson, C. A.-L., et al. (2018). The development of late-stage continental breakup: Seismic reflection and borehole evidence from the Danakil Depression, Ethiopia. *Tectonics*, *37*(9), 2848–2862. https://doi.org/10.1029/2017TC004798

Bastow, I. D., & Keir, D. (2011). The protracted development of the continent-ocean transition in Afar. *Nature Geoscience*, *4*(4), 248–250. https://doi.org/10.1038/ngeo1095

Bedada, T. B. (2010). *An absolute geopotential height system for Ethiopia (Doctoral dissertation)*. University of Edinburgh. Retrieved from Edinburgh Research Archive https://era.ed.ac.uk/handle/1842/4726

Belachew, M., Ebinger, C., Coté, D., Keir, D., Rowland, J. V., Hammond, J. O. S., & Ayele, A. (2011). Comparison of dike intrusions in an incipient seafloor-spreading segment in Afar, Ethiopia: Seismicity perspectives. *Journal of Geophysical Research*, *116*(B6), B06405. https://doi.org/10.1029/2010JB007908

Bell, R. E., Jackson, C. A.-L., Whipp, P. S., & Clements, B. (2014). Strain migration during multiphase extension: Observations from the northern North Sea. *Tectonics*, *33*(10), 1936–1963. https://doi.org/10.1002/2014TC003551

Bellahsen, N., Facenna, C., Funiciello, F., Daniel, J. M., & Jolivet, L. (2003). Why did Arabia separate from Africa? Insights from 3-D laboratory experiments. *Earth and Planetary Science Letters*, *216*(3), 365–381. https://doi.org/10.1016/S0012-821X(03)00516-8

Beyene, A., & Abdelsalam, M. G. (2005). Tectonics of the Afar Depression: A review and synthesis. *Journal of African Sciences*, *41*(1–2), 41–59. https://doi.org/10.1016/j.jafrearsci.2005.03.003

Bonatti, E., Galsperini, E., Vigliotti, L., Lupi, L., Vaselli, O., Polonia, A., & Gasperini, L. (2017). Lake Afrera, a structural depression in the Northern Afar Rift (Red Sea). *Heliyon*, *3*(5), e00301. https://doi.org/10.1016/j.heliyon.2017.e00301

Brune, S. (2016). Rifts and rifted margins: A review of geodynamic processes and natural hazards. In J. C. Duarte & W. P. Schellart (Eds.), *Plate boundaries and natural hazards, AGU geophysical monograph* (Vol. 219, pp. 11–37). American Geophysical Union. https://doi.org/10.1002/9781119054146.ch2

Buck, W. (2006). The role of magma in the development of the Afro-Arabian Rift System. In G. Yirgu, C. J. Ebinger, & P. K. H. Maguire (Eds.), *The Afar volcanic province within the East African Rift system* (Vol. 259, pp. 43–54). Geological Society, London, Special Publications. https://doi.org/10.1144/GSL.SP.2006.259.01.05

Bull, J. M., Minshull, T. A., Mitchell, N. C., Thors, K., Dix, J. K., & Best, A. I. (2003). Fault and magmatic interaction within Iceland's western rift over the last 9 kyr. *Geophysical Journal International*, *154*(1), F1–F8. https://doi.org/10.1046/j.1365-246X.2003.01990.x

Burov, E. B., & Diament, M. (1995). The effective elastic thickness (T_e) of continental lithosphere: What does it really mean? *Journal of Geophysical Research*, *100*(B3), 3905–3927. https://doi.org/10.1029/94JB02770

Canales, J. P., Detrick, R. S., Lin, J., Collins, J. A., & Toomey, D. R. (2000). Crustal and upper mantle seismic structure beneath the rift mountains and across a nontransform offset at the Mid-Atlantic Ridge (35°N). *Journal of Geophysical Research*, *105*(B2), 2699–2719. https://doi.org/10.1029/1999JB900379

Carbotte, S. M., Smith, D. K., Cannat, M., & Klein, E. M. (2016). Tectonic and magmatic segmentation of the Global Ocean Ridge System: A synthesis of observations. In T. J. Wright, A. Ayele, D. J. Ferguson, T. Kidane, & C. Vye-Brown (Eds.), *Magmatic rifting and active volcanism* (Vol. 420, pp. 249–295). Geological Society, London, Special Publications. https://doi.org/10.1144/SP420.5

Corti, G. (2009). Continental rift evolution: From rift initiation to incipient break-up in the Main Ethiopian Rift, East Africa. *Earth-Science Reviews*, *96*(1–2), 1–53. https://doi.org/10.1016/j.earscirev.2009.06.005

Cowie, P. A., Underhill, J. R., Behn, M. D., Lin, J., & Gill, C. E. (2005). Spatio-temporal evolution of strain accumulation derived from multi-scale observations of Late Jurassic rifting in the northern North Sea: A critical test of models for lithospheric extension. *Earth and Planetary Science Letters*, *234*(3–4), 401–419. https://doi.org/10.1016/j.epsl.2005.01.039

Delaney, P. T., Pollard, D. D., Ziony, J. I., & McKee, E. H. (1986). Field relations between dikes and joints: Emplacement processes and paleostress analysis. *Journal of Geophysical Research*, *91*(B5), 4920–4938. https://doi.org/10.1029/JB091iB05p04920

Detrick, R. S., Needham, H. D., & Renard, V. (1995). Gravity anomalies and crustal thickness variations along the MidAtlantic Ridge between 33°N and 40°N. *Journal of Geophysical Research*, *100*(B3), 3767–3787. https://doi.org/10.1029/94JB02649

Drury, S. A., Kelley, S. P., Berhe, S. M., Collier, R. E. L., & Abraha, M. (1994). Structures related to Red Sea evolution in northern Eritrea. *Tectonics*, *13*(6), 1371–1380. https://doi.org/10.1029/94TC01990

Dugda, M., Nyblade, A. A., Julia, J., Langston, C. A., Ammon, C. J., & Simiyu, S. (2005). Crustal structure in Ethiopia and Kenya from receiver function analysis. *Journal of Geophysical Research*, *110*(B1), B01303. https://doi.org/10.1029/2004JB003065

Dumont, S., Klinger, Y., Socquet, A., Doubre, C., & Jacques, E. (2017). Magma influence on propagation of normal faults: Evidence from cumulative slip profiles along Dabbahu-Manda-Hararo rift segment (Afar, Ethiopia). *Journal of Structural Geology*, *95*, 48–59. https://doi.org/10.1016/j.jsg.2016.12.008

Dumont, S., Klinger, Y., Socquet, A., Escartin, J., Grandin, R., Jacques, E., et al. (2019). Rifting process at a continent-ocean transition rift revealed by fault analysis: Example of Dabbahu-Manda-Hararo Rift (Ethiopia). *Tectonics*, *38*(1), 190–214. https://doi.org/10.1029/2018TC005141

Dziewonski, A. M., Chou, T.-A., & Woodhouse, J. H. (1981). Determination of earthquake source parameters from waveform data for studies of global and regional seismicity. *Journal of Geophysical Research*, *86*(B4), 2825–2852. https://doi.org/10.1029/JB086iB04p02825

Eagles, G., Gloaguen, R., & Ebinger, C. (2002). Kinematics of the Danakil microplate. *Earth and Planetary Science Letters*, *203*(2), 607–620. https://doi.org/10.1016/S0012-821X(02)00916-0

Ebinger, C. (2005). Continental break-up: The East African perspective. *Astronomy and Geophysics*, *46*(2), 16–21. https://doi.org/10.1111/j.1468-4004.2005.46216.x

Ebinger, C., Jackson, J. A., Foster, A. N., & Hayward, N. J. (1999). Extensional basin geometry and the elastic lithosphere. *Philosophical Transactions of the Royal Society of London*, *357*(1753), 741–765. https://doi.org/10.1098/rsta.1999.0351

Ebinger, C. J., & Casey, M. (2001). Continental breakup in magmatic provinces: An Ethiopian example. *Geology*, *29*(6), 527–530. https://doi.org/10.1130/0091-7613(2001)029<0527:CBIMPA>2.0.CO;2

Ebinger, C. J., Keir, D., Bastow, I. D., Whaler, K., Hammond, J. O. S., Ayele, A., et al. (2017). Crustal structure of active deformation zones in Africa: Implications for global crustal processes. *Tectonics*, *36*(12), 3298–3332. https://doi.org/10.1002/2017TC004526

Einarsson, P. (2008). Plate boundaries, rifts and transforms in Iceland. *Jökull Journal*, *58*(1), 35–58. https://doi.org/10.33799/jokull2008.58.035

Ekström, G., Nettles, M., & Dziewonksi, A. M. (2012). The global CMT project 2004-2010: Centroid-moment tensors for 13,017 earthquakes. *Physics of the Earth and Planetary Interiors*, *200–201*, 1–9. https://doi.org/10.1016/j.pepi.2012.04.002

Escartín, J., Cowie, P. A., Searle, S., Allerton, S., Mitchell, N. C., MacLeod, C. J., & Slootweg, A. P. (1999). Quantifying tectonic strain and magmatic accretion at a slow spreading ridge segment, Mid-Atlantic Ridge, 29°N. *Journal of Geophysical Research*, *104*(B5), 10421–10437. https://doi.org/10.1029/1998JB900097

Foubert, A., Jaramillo-Vogel, D., Eisenhauer, A., Schaegis, J.-C., Atnafu, B., & Kidane, T. (2015a). Coral reefs and microbial deposits in an active rift setting: Insights from the Danakil Depression (Afar, Ethiopia). Abstract Book Bathurst Meeting 2015.

Foubert, A., Jaramillo-Vogel, D., Eisenhauer, A., Schaegis, J.-C., Atnafu, B., & Kidane, T. (2015b). *SERENA—Sedimentary record of the northern Afar (Ethiopia) coral reefs and microbial deposits in an active rift setting*. 1st International Carbonate Mound Conference 2015. Monte Verita.

Franke, D. (2013). Rifting, lithosphere breakup and volcanism: Comparison of magma-poor and volcanic rifted margins. *Marine and Petroleum Geology*, *43*, 63–87. https://doi.org/10.1016/j.marpetgeo.2012.11.003

Furman, T., Bryce, J., Rooney, T., Hanan, B., Yirgu, G., & Ayalew, D. (2006). Heads and tails: 30 million years of the Afar plume. In G. Yirgu, C. Ebinger, & P. K. H. Maguire (Eds.), *The Afar volcanic province within the East African Rift System* (Vol. 259(1), pp. 95–119). Geological Society, London, Special Publications. https://doi.org/10.1144/GSL.SP.2006.259.01.09

Gawthorpe, R. L., Jackson, C. A.-L., Young, M. J., Sharp, I. R., Moustafa, A. R., & Leppard, C. W. (2003). Normal fault growth, displacement localisation and the evolution of normal fault populations: The Hammam Faraun fault blocks, Suez Rift, Egypt. *Journal of Structural Geology*, *25*(6), 883–895. https://doi.org/10.1016/S0191-8141(02)00088-3

Gawthorpe, R. L., & Leeder, M. R. (2000). Tectono-sedimentary evolution of active extensional basins. *Basin Research*, *12*(3–4), 195–218. https://doi.org/10.1111/j.1365-2117.2000.00121.x

Ghebreab, W., & Talbot, C. (2000). Red Sea extension influenced by PanAfrican tectonic grain in eastern Eritrea. *Journal of Structural Geology*, *22*(7), 931–946. https://doi.org/10.1016/S0191-8141(00)00022-5

Global Volcanism Program. (2022). *Volcanoes of the World, v. 5.0.1*. In E.Venzke (Ed.). Smithsonian Institution. https://doi.org/10.5479/si.GVP.VOTW5-2022.5.0

Green, R. G., White, R. S., & Greenfield, T. (2014). Motion in the North Iceland volcanic rift zone accommodated by bookshelf faulting. *Nature Geoscience*, *7*(1), 29–33. https://doi.org/10.1038/ngeo2012

Hammond, J. O. S., Kendall, J.-M., Stuart, G. W., Keir, D., Ebinger, C., Ayele, A., & Belachew, M. (2011). The nature of the crust beneath the Afar triple junction: Evidence from receiver functions. *Geochemistry, Geophysics, Geosystems*, *12*(12). https://doi.org/10.1029/2011GC003738

Haq, B. U., Hardenbol, J., & Vail, P. R. (1987). Chronology of fluctuating sea levels since the Triassic. *Science*, *235*(4793), 1156–1167. https://doi.org/10.1126/science.235.4793.1156

Hayward, N. J., & Ebinger, C. J. (1996). Variations in the along-axis segmentation of the Afar Rift system. *Tectonics*, *15*(2), 244–257. https://doi.org/10.1029/95TC02292

Hofmann, C., Courtillot, V., Féraud, G., Rochette, P., Yirgu, G., Ketefo, E., & Pik, R. (1997). Timing of the Ethiopian flood basalt event and implications for plume birth and global change. *Nature*, *389*(6653), 838–841. https://doi.org/10.1038/39853

Hooft, E. E. E., Detrick, R. S., Toomey, D. R., Collins, J. A., & Lin, J. (2000). Crustal thickness and structure along three contrasting spreading segments of the Mid-Atlantic Ridge, 33.5°– 35°N. *Journal of Geophysical Research*, *105*(B4), 8205–8226. https://doi.org/10.1029/1999JB900442

Hutchinson, R. W., & Engels, G. G. (1970). Tectonic significance of regional geology and evaporite lithofacies in northeastern Ethiopia. *Philosophical Transactions of the Royal Society of London*, *267*(1181), 313–329. https://doi.org/10.1098/rsta.1970.0038

Illsley-Kemp, F., Bull, J. M., Keir, D., Geyra, T., Pagli, C., Gernon, T. M., et al. (2018). Initiation of a Proto-transform fault prior to seafloor spreading. *Geochemistry, Geophysics, Geosystems*, *19*(12), 4744–4756. https://doi.org/10.1029/2018GC007947

Illsley-Kemp, F., Keir, D., Bull, J. M., Gernon, T. M., Ebinger, C., Ayele, A., et al. (2018). Seismicity during continental breakup in the Red Sea rift of Northern Afar. *Journal of Geophysical Research: Solid Earth*, *123*(3), 2345–2362. https://doi.org/10.1002/2017JB014902

Jackson, J. A., & White, N. J. (1989). Normal faulting in the upper continental crust: Observations from regions of active extension. *Journal of Structural Geology*, *11*(1–2), 15–36. https://doi.org/10.1016/0191-8141(89)90033-3

Jaramillo-Vogel, D., Foubert, A., Braga, J. C., Schaegis, J.-C., Atnafu, B., Grobety, B., & Kidane, T. (2019). Pleistocene sea-floor fibrous crusts and spherulites in the Danakil Depression (Afar, Ethiopia). *Sedimentology*, *66*(2), 480–512. https://doi.org/10.1111/sed.12484

Jolly, R. J. H., & Sanderson, D. J. (1997). A Mohr circle construction for the opening of a pre-existing fracture. *Journal of Structural Geology*, *19*(6), 887–892. https://doi.org/10.1016/S01918141(97)00014-X

Keir, D., Bastow, I. D., Corti, G., Mazzarini, F., & Rooney, T. O. (2015). The origin of along-rift variations in faulting and magmatism in the Ethiopian Rift. *Tectonics*, *34*(3), 464–477. https://doi.org/10.1002/2014TC003698

Keir, D., Bastow, I. D., Pagli, C., & Chambers, E. L. (2013). The development of extension and magmatism in the Red Sea rift of Afar. *Tectonophysics*, *607*, 98–114. https://doi.org/10.1016/j.tecto.2012.10.015

Kirschner, J. P., Kominz, M. A., & Mwankanyamale, K. E. (2010). Quantifying extension of passive margins: Implications for sea level change. *Tectonics*, *29*(4), TC4006. https://doi.org/10.1029/2009TC002557

Kuo, B., & Forsyth, D. W. (1988). Gravity anomalies of the ridge-transform system in the South Atlantic between 31° and 34.5°S: Upwelling centers and variations in crustal thickness. *Marine Geophysical Researches*, *10*(3–4), 205–232. https://doi.org/10.1007/BF00310065

Kurz, T., Gloaguen, R., Ebinger, C., Casey, M., & Abede, B. (2007). Deformation distribution and type in the Main Ethiopian Rift (MER): A remote sensing study. *Journal of African Earth Sciences*, *48*(2–3), 100–114. https://doi.org/10.1016/j.jafrearsci.2006.10.008

Kyser, T. K. (2007). Fluids, basin analysis, and mineral deposits. *Geofluids*, *7*(2), 238–257. https://doi.org/10.1111/j.1468-8123.2007.00178.x

La Rosa, A., Pagli, C., Keir, D., Sani, F., Corti, G., Wang, H., & Possee, D. (2019). Observing oblique slip during rift linakge in northern Afar. *Geophysical Research Letters*, *46*(19), 10782–10790. https://doi.org/10.1029/2019GL084801

La Rosa, A., Pagli, C., Wang, H., Doubre, C., Leroy, S., Sani, F., et al. (2021). Plate-Boundary kinematics of the Afrera linkage zone (Afar) from InSAR and seismicity. *Journal of Geophysical Research: Solid Earth*, *126*(5), e2020JB021387. https://doi.org/10.1029/2020JB021387

Lascialfari, M. (2017). *Quantifying the uncertainty of depth conversion for seismic reflection data from Ethiopia's Danakil Depression*. (MSc exploration geophysics thesis). University of Leeds.

Lavier, L. L., & Manatschal, G. (2006). A mechanism to thin the continental lithosphere at magma-poor margins. *Nature*, *440*(7082), 324–328. https://doi.org/10.1038/nature04608

Le Gall, B., Leleu, S., Pik, R., Jourdan, F., Chazot, G., Ayalew, D., et al. (2018). The Red Beds Series in the Erta Ale segment, North Afar. Evidence for a 6 Ma-old post-rift basin prior to continental rupturing. *Tectonophysics*, *747–748*, 373–389. https://doi.org/10.1016/j.tecto.2018.10.002

Leroy, S., d'Acremont, E., Tiberi, C., Basuyau, C., Autin, J., Lucazeau, F., & Sloan, H. (2010). Recent off-axis volcanism in the eastern Gulf of Aden: Implications for plume-ridge interaction. *Earth and Planetary Science Letters*, *293*(1–2), 140–153. https://doi.org/10.1016/j.epsl.2010.02.036

Levell, B., Argent, J., Dore, G., & Fraser, S. (2011). Passive margins: Overview. In B. A. Vining & S. C. Pickering (Eds.), *Petroleum geology: From mature basins to new frontiers - Proceedings of the 7th petroleum geology conference* (pp. 823–830). https://doi.org/10.1144/0070823

Liu, Z., & Buck, W. R. (2018). Magmatic controls on axial relief and faulting at mid-ocean ridges. *Earth and Planetary Science Letters*, *491*, 226–237. https://doi.org/10.1016/j.epsl.2018.03.045

Liu, Z., & Buck, & W. R. (2020). Global trends of axial relief and faulting at plate spreading centers imply discrete magmatic events. *Journal of Geophysical Research: Solid Earth*, *125*(8), e2020JB019465. https://doi.org/10.1029/2020JB019465

López-García, J. M., Moreira, D., Benzerara, K., Grunewald, O., & López-García, P. (2020). Origin and evolution of the halo-volcanic complex of Dallol: Proto-volcanism in Northern Afar (Ethiopia). *Frontiers of Earth Science*, *7*, 351. https://doi.org/10.3389/feart.2019.00351

Macdonald, K. C., Fox, P., Perram, L., Eisen, M., Haymon, R., Miller, S., et al. (1988). A new view of the mid-ocean ridge from the behaviour of ridge-axis discontinuities. *Nature*, *335*(6187), 217–225. https://doi.org/10.1038/335217a0

Maguire, P. K. H., Keller, G. R., Klemperer, S. L., Mackeznie, G. D., Keranen, K., Harder, S., et al. (2006). Crustal structure of the northern Main Ethiopian rift from the EAGLE controlled-source survey; a snapshot of incipient lithospheric break-up. *Geological Society, London, Special Publication*, *259*(1), 269–291. https://doi.org/10.1144/GSL.SP.2006.259.01.21

Makris, J., & Ginzburg, A. (1987). The Afar depression: Transition between continental rifting and sea-floor spreading. *Tectonophysics*, *141*(1–3), 199–214. https://doi.org/10.1016/0040-1951(87)90186-7

Manighetti, I., Tapponnier, P., Courtillot, V., Gallet, Y., Jaques, E., & Gillot, P.-Y. (2001). Strain transfer between disconnected, propagating rifts in Afar. *Journal of Geophysical Research*, *106*(B7), 13613–13665. https://doi.org/10.1029/2000JB900454

McClusky, S., Reilinger, R., Ogubazghi, G., Amleson, A., Healeb, B., Vernant, P., et al. (2010). Kinematics of the southern Red Sea–Afar triple junction and implications for plate dynamics. *Geophysical Research Letters*, *37*(5). https://doi.org/10.1029/2009GL041127

McCoss, A. M. (1986). Simple constructions for deformation in transpression/transtension zones. *Journal of Structural Geology*, *8*(6), 715–718. https://doi.org/10.1016/0191-8141(86)90077-5

McKenzie, D., Davies, D., & Molnar, P. (1970). Plate tectonics of the Red Sea and East Africa. *Nature*, *226*(5242), 243–248. https://doi.org/10.1038/226243a0

McKenzie, D., Jackson, J., & Priestly, K. (2005). Thermal structure of oceanic and continental lithosphere. *Earth and Planetary Science Letters*, *223*(3–4), 337–349. https://doi.org/10.1016/j.epsl.2005.02.005

Moore, C., Wright, T., Hooper, A., & Biggs, J. (2019). The 2017 eruption of Erta'Ale volcano, Ethiopia: Insights into the shallow axial plumbing system of an incipient mid-ocean ridge. *Geochemistry, Geophysics, Geosystems*, *20*(12), 5727–5743. https://doi.org/10.1029/2019GC008692

Muirhead, J. D., Kattenhorn, S. A., Lee, H., Mana, S., Turrin, B. D., Fischer, T. P., et al. (2016). Evolution of upper crustal faulting assisted by magmatic volatile release during early-stage continental rift development in the East African Rift. *Geosphere*, *12*(6), 1670–1700. https://doi.org/10.1130/GES01375.1

Nixon, C. W., McNeill, L. C., Bull, J. M., Bell, R. E., Gawthorpe, R. L., Henstock, T. J., et al. (2016). Rapid spatiotemporal variations in rift structure during development of the Corinth Rift, central Greece. *Tectonics*, *35*(5), 1225–1248. https://doi.org/10.1002/2015TC004026

Nobile, A., Pagli, C., Keir, D., Wright, T. J., Ayele, A., Ruch, J., & Acocella, V. (2012). Dike-fault interaction during the 2004 Dallol intrusion at the northern edge of the Erta Ale Ridge (Afar, Ethiopia). *Geophysical Research Letters*, *39*(19). https://doi.org/10.1029/2012GL053152

Nyberg, B., Nixon, C. W., & Sanderson, D. J. (2018). NetworkGT: A GIS tool for geometric and topological analyses of two-dimensional fracture networks. *Geosphere*, *14*(4), 1618–1634. https://doi.org/10.1130/GES01595.1

Pagli, C., Wright, T. J., Ebinger, C. J., Yun, S.-H., Cann, J. R., Barnie, T., & Atalay, A. (2012). Shallow axial magma chamber at the slow spreading Erta Ale Ridge. *Nature Geoscience*, *5*(4), 284–288. https://doi.org/10.1038/ngeo1414

Pagli, C., Yun, S.-H., Ebinger, C., Keir, D., & Wang, H. (2018). Strike-slip tectonics during rift linkage. *Geology*, *47*(1), 31–34. https://doi.org/10.1130/g45345.1

Peron-Pinvidic, G., & Manatschal, G. (2009). The final rifting evolution at deep magma-poor passive margins from Iberia-Newfoundland: A new point of view. *International Journal of Earth Sciences*, *98*(7), 1581–1597. https://doi.org/10.1007/s00531-008-0337-9

Peron-Pinvidic, G., Manatschal, G., & Osmundsen, P. T. (2013). Structural comparison of archetypal Atlantic rifted margins: A review of observations and concepts. *Marine and Petroleum Geology*, *43*, 21–47. https://doi.org/10.1016/j.marpetgeo.2013.02.002

Phipps Morgan, J., & Chen, Y. J. (1993). Dependence of ridge-axis morphology on magma supply and spreading rate. *Nature*, *364*(6439), 706–708. https://doi.org/10.1038/364706a0

Reston, T. J. (2009). The extension discrepancy and syn-rift subsidence deficit at rifted margins. *Petroleum Geoscience*, *15*(3), 217–237. https://doi.org/10.1144/1354-079309-845

Robertson, E. A. M., Biggs, J., Cashman, K. V., Floyd, M. A., & Vye-Brown, C. (2016). Influence of regional tectonics and pre-existing structures on the formation of elliptical calderas in the Kenyan Rift. In T. J. Wright, A. Ayele, D. J. Ferguson, T. Kidane, & C. Vye-Brown (Eds.), *Magmatic rifting and active volcanism* (Vol. 420, pp. 43–67). Geological Society, London, Special Publications. https://doi.org/10.1144/SP420.12

Rogers, N., MacDonald, R., Fitton, J. G., George, R., Smith, M., & Barreiro, B. (2000). Two mantle plumes beneath the East African rift system: Sr, Nd and Pb isotope evidence from Kenya Rift basalts. *Earth and Planetary Science Letters*, *176*(3–4), 387–400. https://doi.org/10.1016/S0012-821X(00)00012-1

Rooney, T. O. (2017). The Cenozoic magmatism of East Africa: Part I – Flood basalts and pulsed magmatism. *Lithos*, *286–287*, 264–301. https://doi.org/10.1016/j.lithos.2017.05.014

Rowland, J. V., Baker, E., Ebinger, C. J., Keir, D., Kidane, T., Biggs, J., et al. (2007). Fault growth at a nascent slow-spreading ridge: 2005 Dabbahu rifting episode, Afar. *Geophysical Journal International*, *171*(3), 1226–1246. https://doi.org/10.1111/j.1365-246X.2007.03584.x

Ruch, J., Wang, T., Xu, W., Hensch, M., & Jónsson, S. (2016). Oblique rift opening revealed by reoccurring magma injection in central Iceland. *Nature Communications*, *7*(1), 12352. https://doi.org/10.1038/ncomms12352

Schaegis, J.-C., Rime, V., Kidane, T., Mosar, J., Gebru, E. F., Atnafu, B., & Foubert, A. (2021). Novel bathymetry of Lake Afdera reveals fault structures and volcano-tectonic features of an incipient transform zone (Afar, Ethiopia). *Frontiers of Earth Science*, *9*, 706643. https://doi.org/10.3389/feart.2021.706643

Scholz, C. H., & Contreras, J. C. (1998). Mechanics of continental rift architecture. *Geology*, *26*(11), 967–970. https://doi.org/10.1130/0091-7613(1998)026<0967:MOCRA>2.3.CO;2

Shaw, P. R. (1992). Ridge segmentation, faulting, and crustal thickness in the Atlantic. *Nature*, *358*(6386), 490–493. https://doi.org/10.1038/358490a0

Shaw, P. R., & Lin, J. (1993). Causes and consequences of variations in faulting style at the Mid-Atlantic Ridge. *Journal of Geophysical Research*, *98*(B12), 21839–21851. https://doi.org/10.1029/93JB01565

Shillington, D. J., Scott, C. L., Minshull, T. A., Edwards, R. A., Brown, P. J., & White, N. (2009). Abrupt transition from magma-starved to magma-rich rifting in the eastern Black Sea. *Geology*, *37*(1), 7–10. https://doi.org/10.1130/G25302A.1

Siegburg, M., Bull, J. M., Nixon, C. W., Keir, D., Gernon, T. M., Corti, G., et al. (2020). Quantitative constraints on faulting and fault slip-rates in the northern Main Ethiopian Rift. *Tectonics*, *39*(8), e2019TC006046. https://doi.org/10.1029/2019TC006046

Stab, M., Bellahsen, N., Pik, R., Quidelleur, X., Ayalew, D., & Leroy, S. (2016). Modes of rifting in magma-rich setting: Tectono-magmatic evolution of Central Afar. *Tectonics*, *35*(1), 2–38. https://doi.org/10.1002/2015TC003893

Stuart, G. W., Bastow, I. D., & Ebinger, C. J. (2006). Crustal structure of the northern Main Ethiopian Rift from receiver function studies. In G. Yirgu, C. Ebinger, & P. K. H. Maguire (Eds.), *The Afar volcanic province within the East African Rift system* (Vol. 259(1), pp. 253–267). Geological Society, London, Special Publications. https://doi.org/10.1144/GSL.SP.2006.259.01.20

Szymanski, E., Stockli, D. F., Johnson, P. R., & Hager, C. (2016). Thermochronometric evidence for diffuse extension and two-phase rifting within the Central Arabian Margin of the Red Sea Rift. *Tectonics*, *35*(12), 2863–2895. https://doi.org/10.1002/2016TC004336

Taylor, B., Weiss, J. R., Goodliffe, A. M., Sachpazi, M., Laigle, M., & Hirn, A. (2011). The structures, stratigraphy and evolution of the Gulf of Corinth rift, Greece. *Geophysical Journal International*, *185*(3), 1189–1219. https://doi.org/10.1111/j.1365-246X.2011.05014.x

Tesauro, M., Audet, P., Kaban, M. K., Bürgmann, R., & Cloetingh, S. (2012). The effective elastic thickness of the continental lithosphere: Comparison between rheological and inverse approaches. *Geochemistry, Geophysics, Geosystems*, *13*(9), Q09001. https://doi.org/10.1029/2012GC004162

Tesfaye, S., Harding, D., & Kusky, T. (2003). Early continental breakup boundary and migration of the Afar triple junction, Ethiopia. *Geological Society of America Bulletin*, *115*(9), 1053–1067. https://doi.org/10.1130/B25149.1

Thurmond, A. K., Abdelsalam, M. G., & Thurmond, J. B. (2006). Optical-radar-DEM remote sensing data integration for geological mapping in the Afar Depression, Ethiopia. *Journal of African Earth Sciences*, *44*(2), 119–134. https://doi.org/10.1016/j.jafrearsci.2005.10.006

Tiberi, C., Ebinger, C., Ballu, V., Stuart, G., & Oluma, B. (2005). Inverse models of gravity data from the Red Sea-Aden-East African rifts triple junction zone. *Geophysical Journal International*, *163*(2), 775–787. https://doi.org/10.1111/j.1365-246X.2005.02736.x

Tuckwell, G. W., Bull, J. M., & Sanderson, D. J. (1996). Models of fracture orientation at oblique spreading centres. *Journal of the Geological Society*, *153*(2), 185–189. https://doi.org/10.1144/gsjgs.153.2.0185

Tugend, J., Gillard, M., Manatschal, G., Nirrengarten, M., Harkin, C., Epin, M.-E., et al. (2018). Reappraisal of the magma-rich versus magma-poor rifted margin archetypes. In K. R. McClay & J. A. Hammerstein (Eds.), *Passive margins: Tectonic, sedimentation and magmatism* (Vol. 476, pp. 23–47). Geological Society, London, Special Publications. https://doi.org/10.1144/SP476.9

Ukstins, I. A., Renne, P. R., Wolfenden, E., Baker, J., Ayalew, D., & Menzies, M. (2002). Matching conjugate volcanic rifted margin: $^{40}Ar/^{39}Ar$ chrono-stratigraphy of pre- and syn-rift bimodal flood volcanism in Ethiopia and Yemen. *Earth and Planetary Science Letters*, *198*(3–4), 289–306. https://doi.org/10.1016/S0012-821X(02)00525-3

Villemin, T., & Bergerat, F. (2013). From surface fault traces to a fault growth model: The Vogar Fissure Swarm of the Reykjanes Peninsula, Southwest Iceland. *Journal of Structural Geology*, *51*, 38–51. https://doi.org/10.1016/j.jsg.2013.03.010

Viltres, R., Jónsson, S., Ruch, J., Doubre, C., Reilinger, R., Floyd, M., & Ogubazghi, G. (2020). Kinematics and deformation of the southern Red Sea region from GPS observations. *Geophysical Journal International*, *221*(3), 2143–2154. https://doi.org/10.1093/gji/ggaa109

Watts, E. J., Gernon, T. M., Taylor, R. N., Keir, D., Siegburg, M., Jarman, J., et al. (2020). Evolution of the Alu-Dalafilla and Borale volcanoes, Afar, Ethiopia. *Journal of Volcanology and Geothermal Research*, *408*, 107094. https://doi.org/10.1016/j.jvolgeores.2020.107094

Wessel, P., Luis, J. F., Uieda, L., Scharroo, R., Wobbe, F., Smith, W. H. F., & Tian, D. (2019a). The generic mapping tools version 6 [Software]. Zenodo, *20*, (11), 5556–5564. https://doi.org/10.5281/zenodo.3407866

Wessel, P., Luis, J. F., Uieda, L., Scharroo, R., Wobbe, F., Smith, W. H. F., & Tian, D. (2019b). The generic mapping tools version 6. *Geochemistry, Geophysics, Geosystems*, *20*(11), 5556–5564. https://doi.org/10.1029/2019gc008515

Whitmarsh, R. B., Manatschal, G., & Minshull, T. A. (2001). Evolution of magma-poor continental margins from rifting to seafloor spreading. *Nature*, *413*(6852), 150–154. https://doi.org/10.1038/35093085

Wolfenden, E., Ebinger, C., Yirgu, G., Renne, P. R., & Kelley, S. P. (2005). Evolution of a volcanic rifted margin: Southern Red Sea, Ethiopia. *Geological Society of Amercia Bulletin*, *117*(7–8), 846–864. https://doi.org/10.1130/B25516.1

Xu, W., Rivalta, E., & Li, X. (2017). Magmatic architecture within a rift segment: Articulate axial magma storage at Erta-Ale volcano, Ethiopia. *Earth and Planetary Science Letters*, *476*, 79–86. https://doi.org/10.1016/j.epsl.2017.07.051

Zou, C., Zhai, G., Zhang, G., Wang, H., Zhang, G., Li, J., et al. (2015). Formation, distribution, potential and prediction of global conventional and unconventional hydrocarbon resources. *Petroleum Exploration and Development*, *42*(1), 14–28. https://doi.org/10.1016/S1876-3804(15)60002-7

Zwaan, F., Corti, G., Keir, D., Sani, F., Muluneh, A., Illsley-Kemp, F., & Papini, M. (2020). Geological data from the Western Afar margin, East Africa. [Dataset]. GFZ Data Services. https://doi.org/10.5880/fidgeo.2020.017

Zwaan, F., Corti, G., Sani, F., Keir, D., Muluneh, A. A., Illsley-Kemp, F., & Papini, M. (2020). Structural analysis of the Western Afar margin, East Africa: Evidence for multiphase rotational rifting. *Tectonics*, *39*(7), e2019TC006043. https://doi.org/10.1029/2019TC006043